

# **Magnetic fabrics of rhyolite ignimbrites reveal complex emplacement dynamics of pyroclastic density currents, an example from the Altenberg–Teplice Caldera, Bohemian Massif**

Petr Vitouš<sup>1,2\*</sup>, Filip Tomek<sup>1,2</sup>, Michael S. Petronis<sup>1,3</sup>

<sup>1</sup> *Institute of Geology and Paleontology, Faculty of Science, Charles University, Prague, Czech Republic*

<sup>2</sup> *Czech Academy of Sciences, Institute of Geology, Prague, Czech Republic*

<sup>3</sup> *Environmental Geology, Natural Resources Management Department, New Mexico Highlands University, Las Vegas, New Mexico, 87701, USA*

## **ORCID**

Petr Vitouš 0000-0002-0884-537X

Filip Tomek 0000-0002-1040-0193

Michael S. Petronis 0000-0002-4112-1787

## **TWITTER**

Filip Tomek @FilipTomekGeo

This paper has been accepted as an original research article in *Bulletin of Volcanology* and was submitted as a pre-print to EarthArXiv.

---

\*corresponding author: vitouspe@natur.cuni.cz

## Abstract

The anisotropy of magnetic susceptibility (AMS) is commonly used to infer the flow dynamics, source areas, and post-emplacement processes of pyroclastic density currents (PDC) of young calderas (i.e. Cenozoic). At older calderas, the primary record is often obscured by post-emplacement deformation and/or long-term erosion. Here, we focus on the ~314–313 Ma welded ignimbrites inside the Altenberg–Teplice Caldera (ATC; Bohemian Massif). The small-volume, moderately-welded ignimbrites emplaced prior to caldera-forming eruption yield a generally westward flow direction as determined from the imbrication of the magmatic and magnetic foliation plane. Their eruptive vents were located along the eastern margin of the future caldera. The most voluminous high-grade ignimbrites, products of the caldera-forming event, indicate a high degree of welding and rheomorphic ductile folding that obscured the primary flow fabrics. Based on the fabric pattern, published radiometric and field geology data from the ATC, we interpret that these ignimbrites were sourced from a dike swarm along the northwestern caldera rim. The PDCs then flowed across the subsiding caldera towards the south and south-southeast, where extra-caldera ignimbrites are exposed. The final trap-door caldera collapse triggered the emplacement of the microgranite ring dikes. These dikes, along with the post-caldera granites, may have driven a local resurgence along the eastern caldera rim. As exemplified by the ATC, the AMS fabric can be applied successfully to much older caldera ignimbrites including those with a high degree of welding and rheomorphism to interpret flow direction, deposition, emplacement, and post-emplacement dynamics.

**Keywords:** Anisotropy of magnetic susceptibility (AMS); Collapse caldera; Rhyolite ignimbrite; Pyroclastic density current (PDC); Welding; Resurgence

## 1 Introduction

Pyroclastic density currents (PDCs) are a mixture of volcanic ash, gases, crystals, and juvenile and lithic clasts triggered by the collapse of an eruption column (e.g., Sparks et al. 1973; Sparks and Wilson 1976; Fischer and Schmincke 1984; Branney and Kokelaar 1992, 2002; Giordano and Cas 2021). After the emplacement, they form complex deposits collectively referred to as an ignimbrite (Ross and Smith 1961; Sparks et al. 1973; Sparks 1976; Sparks and Wilson 1976; Walker 1983; Branney and Kokelaar 1992, 2002; Druitt 1998). PDCs are commonly associated with cataclysmic caldera-forming eruptions and, in

exceptional cases, a PDC can travel over 100 km from its source (Chapin and Lowell 1979; Druitt and Sparks 1984; Roche and Druitt 2001; Roche et al. 2016).

Numerous studies have agreed that magnetic fabrics along with the macroscopic petrographic markers allow determining the source vents, flow directions, and syn- to post-emplacement processes such as welding and rheomorphism (e.g., Cagnoli and Tarling 1997; Ort et al. 1999, 2003, 2013, 2015; Pioli et al. 2008; LaBerge et al. 2009; Petronis and Geissman 2009; Geissman et al. 2010; Cañón-Tapia and Mendoza-Borunda 2014; Agrò et al. 2015). Most of these studies focused on Cenozoic volcanic systems, whereas paleovolcanic reconstructions of older Mesozoic, Paleozoic, or even Precambrian calderas and their eruptive products are scarce (Wang et al. 2001; Sohn et al. 2009; Willcock et al. 2015; Hong et al. 2019; Gambeta et al. 2021). This is likely due to the poor exposure of such rocks, significant amounts of erosion, and tectonic overprints.

In this contribution, we focus on the ~314–313 Ma Teplice rhyolite (TR) of the late Carboniferous Altenberg–Teplice Caldera (ATC) in NW Bohemian Massif at the Czech/German border (Fig. 1a). The caldera activity was synchronous with the terminal collapse phase of the Variscan orogeny (Förster et al. 1999; Štemprok et al. 2003; Tomek et al. 2022) and was not affected by younger ductile deformation. The TR represents a deeply eroded proximal caldera facies dominated by welded ignimbrites and associated ash-fall tuffs, lava flows, and volcanoclastic rocks (Figs. 1a and 2a; Jiránek et al. 1987; Casas-García et al. 2019). We examined the TR through detailed geological mapping, petrographic analyses, and magnetic fabrics determined by the anisotropy of magnetic susceptibility (AMS; e.g., Hrouda 1982; Tarling and Hrouda 1993). Our results reveal the migration of volcanic vents and changes in PDCs flow directions in time. The older and small-volume ignimbrites have dominantly westward flow directions and were sourced from the area along the eastern rim of the future caldera. The younger and more voluminous ignimbrites, products of major caldera-forming eruptions, yield a more complex magnetic fabric pattern interpreted as rheomorphic folding. These ignimbrites indicate a north-northeast flow direction sourced dominantly from a dike swarm along the northern caldera periphery along with some scattered vents within the caldera.

## 2 Geological setting

### 2.1 Altenberg–Teplice Caldera

The late Carboniferous ATC is located in the NW Bohemian Massif, eastern Variscan belt (Fig. 1a). The  $\sim 36 \times 18$  km caldera is elongated in  $\sim$ NNW–SSE direction. Approximately one-third of the caldera to the south is covered by younger volcanic and sedimentary rocks (Mlčoch and Skácelová 2010). The caldera is an asymmetric trapdoor with the maximum subsidence and maximum thickness of volcanic deposits in the eastern and southeastern parts (Fig. 1b and c; Jiránek et al. 1987; Benek 1991).

The ATC comprises several plutonic and volcanic units dated from the oldest to youngest based on cross-cutting relations, U-Pb zircon geochronology, and biostratigraphy (Fig. 1a and c). The evolution of the ATC started with the intrusion of the Sayda-Berggießhübel rhyolite dike swarm. The swarm was associated with the onset of the caldera-forming activity and likely represents one of the possible vent locations that erupted the TR (Fig. 1a; Winter et al. 2008). The TR preserved inside the present-day caldera includes various felsic pyroclastic rocks and lava flows intercalated with volcano-sedimentary horizons (e.g., Fiala 1960; Lobin 1986; Jiránek et al. 1987); the TR is described in greater detail below. Termination of the volcanic activity is evidenced by the emplacement of the syn-collapse ring dike system (Tomek et al. 2019) and by the post-collapse granites (Fig. 1a–c; Breiter 2012; Štemprok 2016).

The U-Pb zircon dating indicates a wide spread of ages  $\sim 318$  Ma and  $\sim 314$  Ma (LA–ICP–MS and CA–ID–TIMS; Opluštil et al. 2016; Casas-García et al. 2019; Tomek et al. 2022), which is rather unrealistically long time-span for caldera magmatism. The most data are, however, clustered between  $\sim 314$ – $313$  Ma (Tichomirowa et al. 2022). The major eruption that triggered the final trap-door caldera collapse occurred at  $\sim 313.83$ – $313.41$  Ma (Opluštil et al. 2016). This time span corresponds to the deposition of the correlative extra caldera ignimbrites and ash-fall tuff within the Central Bohemian Carboniferous basins (Tomek et al. 2022). The emplacement of the caldera ring dike system is dated at  $312 \pm 4$  Ma and  $312 \pm 3$  Ma (LA–ICP–MS, U-Pb on zircons; Tomek et al. 2019), and  $314.3 \pm 0.4$  Ma and  $313.1 \pm 0.5$  Ma (CA–ID–TIMS, U-Pb on zircons; Tichomirowa et al. 2022), which overlaps within the analytical error with the age of the caldera-forming eruption.

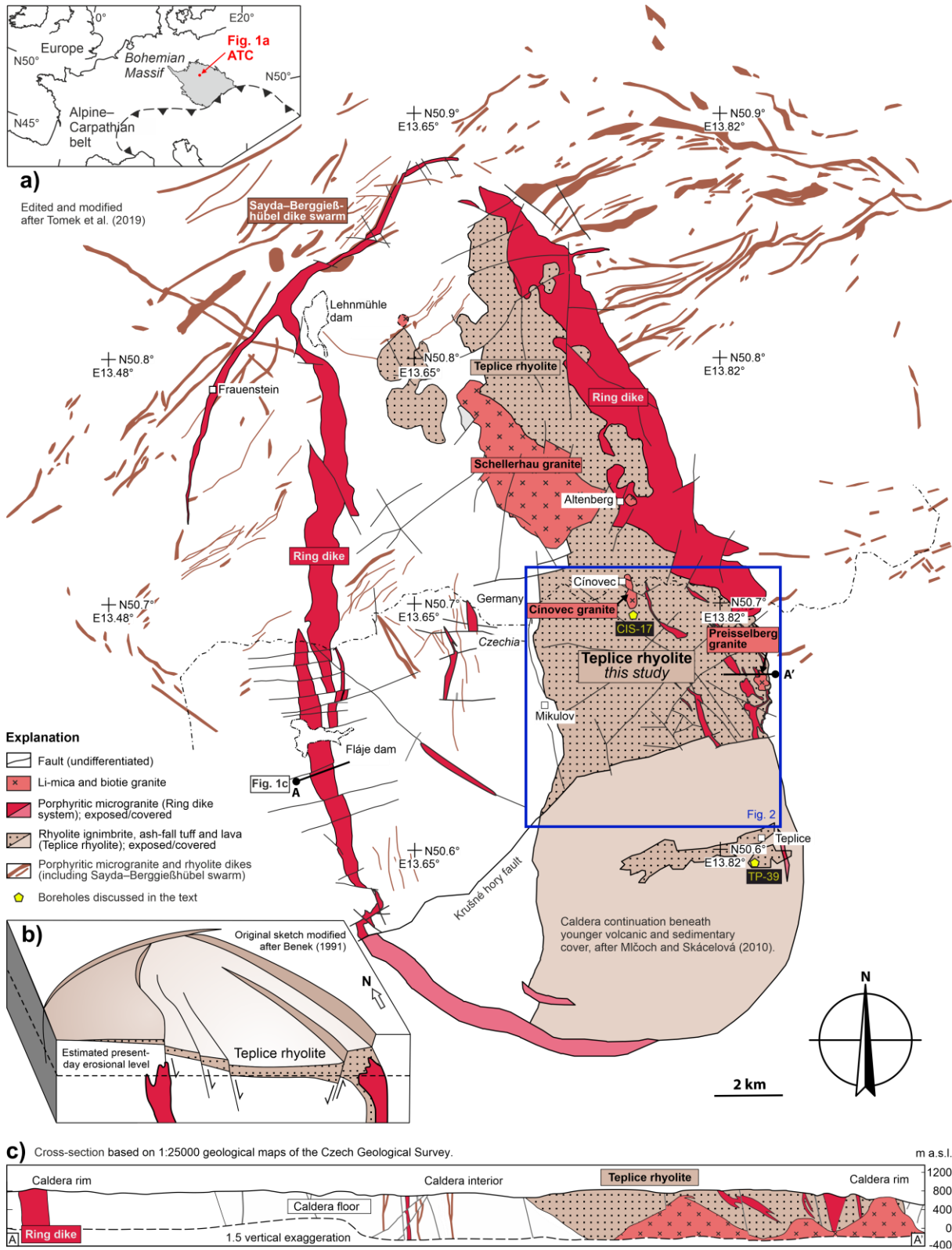


**Figure 1** a) Simplified geologic map of the ATC; the blue square shows the area of interest; see inset for location; b) interpretative model of the trap-door caldera subsidence; c) E–W cross-section through the southern portion of the caldera

## 2.2 Teplice rhyolite

At the present-day erosional level, the TR occupies the eastern third of the caldera and includes rhyolite to rhyodacite ash-fall tuffs, ignimbrites, lava flows, and domes (Figs. 1a and 2a). Based on the whole-rock major and trace element geochemistry, these rocks were likely sourced from a reversely zoned magma chamber (Breiter et al. 2001). The studied area of the TR is divided here into an eastern and a western zone. The eastern zone is intensely intruded by younger post-caldera dikes and granites, whereas the western zone lacks younger intrusions (Fig. 2a). Benek (1991) and Jiránek et al. (1987) interpreted that the volcanic rocks young generally from the west to the east due to the trap-door caldera tilt (Fig. 1b and c). Based on geochemistry alone, without any structural data, Casas-García et al. (2019) suggested that the caldera fill forms a syncline with the youngest members in its core. The correlative extra-caldera ignimbrite deposits were identified ca. 40 km south of the ATC in separate outcrops (Casas-García et al. 2019; Tomek et al. 2022) and a few boreholes (Žáček and Škoda 2009; Opluštil et al. 2016). Tomek et al. (2022) correlated some ash-fall tuff layers in the Carboniferous late-orogenic basins with the TR.

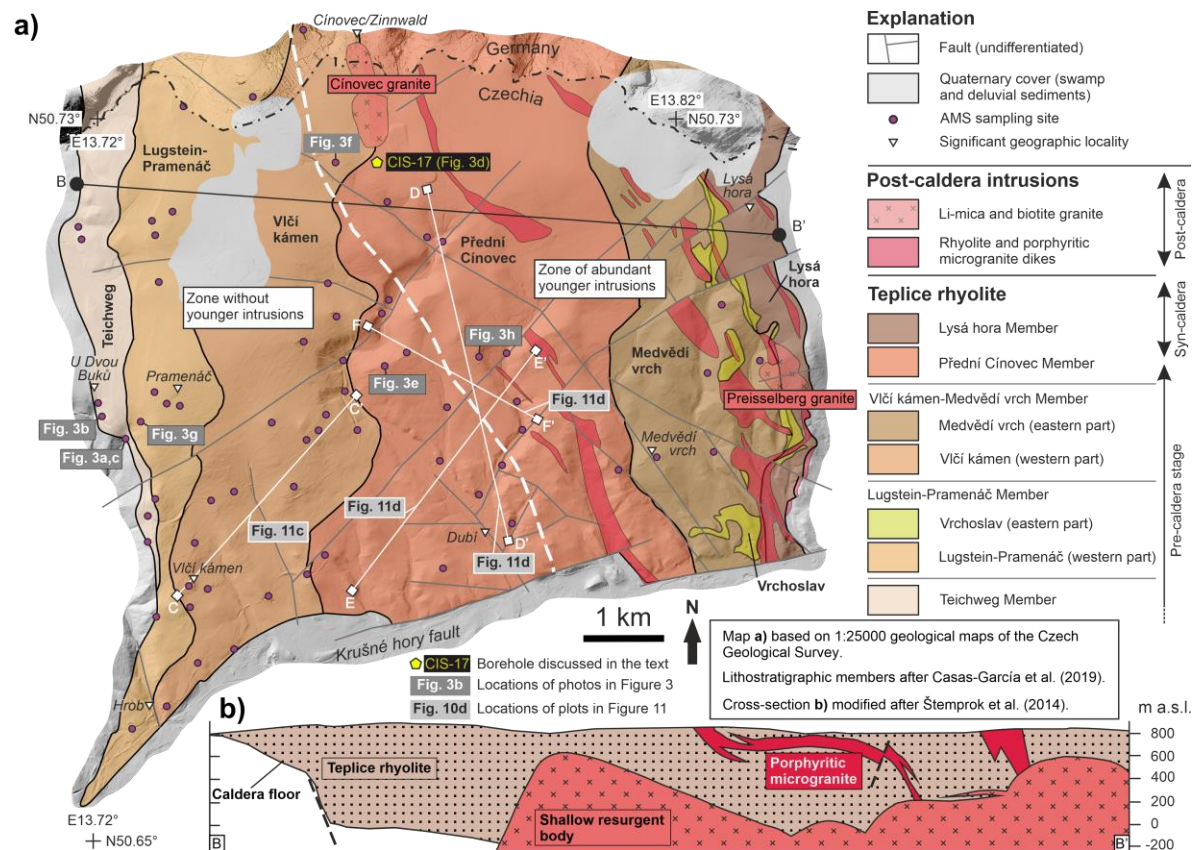


**Figure 2** a) Geological map of the examined part of the TR highlighting locations of AMS sampling sites, and cross-sections are shown in Figure 2b (black lines) and Figure 11b–d (white lines); base shaded relief map layers are freely available through WMS services on Czech Cadastre of Real Estate, and State Enterprise Geobase Information and Surveying of Saxony webpages; b) E–W cross-section through the Teplice rhyolite and adjacent rocks

ID	Lithostratigraphic Member	Shortcode	Lithology
9	Lysá hora	LH	Coherent phenocryst-rich rhyolite lava containing spherulites
8	<b>Přední Cínovec</b>	<b>PC</b>	Poorly sorted, massive, very phenocryst-rich welded trachyte to rhyolite ignimbrite
7	<b>Medvědí vrch (eastern part)</b>	<b>MV</b>	Poorly sorted, massive, very phenocryst-rich welded rhyolite ignimbrite
	<b>Vlčí kámen (western part)</b>	<b>VK</b>	Poorly sorted, massive, very phenocryst-rich welded rhyolite ignimbrite
6	Vrchoslav (eastern part)	Vr	Poorly sorted, massive, very phenocryst-rich welded rhyolite ignimbrite
	<b>Lugstein-Pramenáč (western part)</b>	<b>LP</b>	Poorly sorted, massive, very phenocryst-rich welded rhyolite ignimbrite
5	Altenberg	Al	Poorly sorted, massive, lithic- and phenocryst-rich rhyolite ignimbrite with abundant fiamme
4	<b>Teichweg</b>	<b>Te</b>	Bedded ash-fall tuff overlain by lithic- and phenocryst-rich rhyolite ignimbrite with abundant pumice clasts and fiamme
Volcano-sedimentary horizon 2			
3	Buschmühle B	BuB	Coherent rhyolite lava
	Buschmühle A	BuA	Fallout deposit overlain by phenocryst-rich to lithic-rich ignimbrite
Volcano-sedimentary horizon 1			
2	Schmiedeberg B	ScB	Coherent rhyolite lava
	Schmiedeberg A	ScA	Lithic- and phenocryst-rich rhyolite ignimbrite
1	Barmenberg	Ba	Massive, poorly sorted phenocryst-rich rhyolite ignimbrite

\* lithostratigraphic members highlighted in bold are in focus of this study

**Table 1** Brief lithological summary of the Teplice rhyolite

Based on the historic literature (Moesta 1928; Fiala 1960; Eisenreich and Jeřábek 1978; Holub 1980; Lobin 1986; Jiránek et al. 1987; Benek 1991), Gnojek et al. (2018) and Casas-García et al. (2019) defined nine TR lithostratigraphic members separated by two volcano-sedimentary horizons. The first six members, of minor areal extent at the present-day erosional level, mark the ignimbrite eruptions prior to the final caldera collapse (Tab. 1). The younger and more voluminous members are likely products of initial caldera subsidence (member 7) and caldera-forming event (members 8–9), after which the final trap-door collapse occurred (Tab. 1; Tomek et al. 2019, 2022).

Here, we provide a summary of the lithological description of individual TR members in Table 1 (see Casas-García et al. 2019 for additional details). We focus on the members

Teichweg (4), Lugstein-Pramenáč (6), Vlčí kámen-Medvědí vrch (7), and Přední Cínovec (8), which outcrop superbly on the southern flank of the Krušné hory/Erzgebirge Mts.

The Teichweg Member consists of a basal ash-fall tuff overlain by an ignimbrite (Fig. 3a). This pale-white to greenish ash-fall tuff is very fine-grained and characterized by apparent bedding that dips  $\sim 30^\circ$  to the east-southeast. The moderate degree of welding was interpreted from the careful petrographic observations of Casas García et al. (2019). The ignimbrite displays a compaction flow foliation defined by asymmetric and flattened greenish fiamme (Fig. 3b and c), which distinguishes the Teichweg from the younger TR members. The Lugstein-Pramenáč, Vlčí kámen-Medvědí vrch, and Přední Cínovec members are petrographically similar high-grade (high-degree of welding) ignimbrites (Tab. 1; Casas García et al. 2019). For the purpose of this study, we have divided the Vlčí kámen-Medvědí vrch Member into a western part, Vlčí kámen, and an eastern part, Medvědí vrch (Tab. 1 and Fig. 2a). These reddish to brownish ignimbrites are poor in lithics yet rich in quartz (nevaditic), and only rarely contain larger fiamme (Fig. 3e–h). In detail, they include eutaxitic microstructure with abundant micro-scale recrystallized fiamme, microphenocrysts of biotite, pyroxene, and opaque minerals. The opaque minerals, likely Fe-Ti oxides, constitute relatively large (50–200  $\mu\text{m}$ ) and separate microphenocrysts embedded in the matrix showing no mineral clusters (Fig. 3f–h).

The recent drilling for lithium in the area of the Cínovec pluton (borehole CIS-17) revealed one location of the Přední Cínovec member with abundant larger fiamme and lithic clasts (Fig. 3d). Similar features including intrusions of thin microgranite dikes were detected in the borehole TP-39 (Gnojek et al. 2018).

### 3 Methodology

For a quantification of the internal fabrics of the TR, the AMS was used (e.g., Hrouda 1982; Tarling and Hrouda 1993). The AMS data are visualized through the magnetic fabric ellipsoid defined by three principal susceptibility axes: maximum  $k_1$  (magnetic lineation), intermediate  $k_2$ , and minimum  $k_3$  (pole/normal to the magnetic foliation plane). Three statistical parameters are used to describe the magnetic fabric. The mean (bulk) susceptibility ( $k_m$ ) is controlled by the mineral composition, applied field, mineral abundance, relative mineral proportions, and the domain state of the dominant susceptibility-bearing minerals present within the samples.



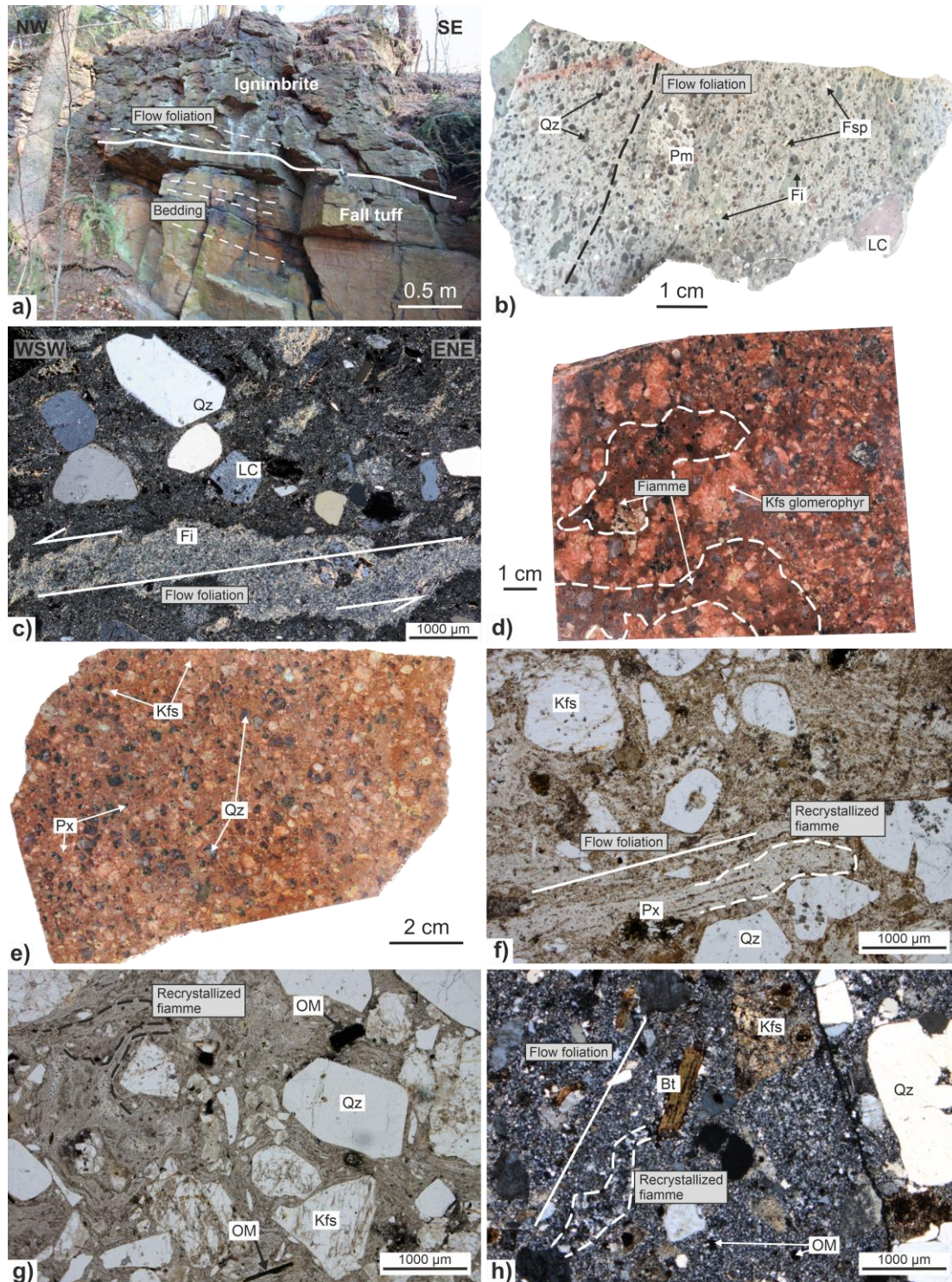


**Figure 3** Photodocumentation of the TR ignimbrites: a) contact of bedded ash-fall tuff and overlying ignimbrite with flow foliation at an angle to contact and bedding, Teichweg Member, site FT001; b) polished slab of the Teichweg pumice- and fiamme-rich ignimbrite with flow foliation defined by shape preferred orientation of flattened fiamme, site FT105; c) cross-polarized microphotograph of the Teichweg ignimbrite showing asymmetric fiamme, site FT001; d) polished slab of a drill-core CIS-17 in the Přední Cínovec ignimbrite with abundant large fiamme; e) polished slab of the typical crystal-rich and fiamme-poor Přední Cínovec ignimbrite, site FT081; plane-polarized microphotographs of f) the Vlčí kámen ignimbrite at site FT089, and g) Lugstein-Pramenáč ignimbrite at site FT090 showing eutaxitic microstructure with micro-scale recrystallized fiamme; h) cross-polarized microphotograph of the Přední Cínovec ignimbrite showing presence of larger Bt grains and recrystallized fiamme, sample FT084; Fi – fiamme; Kfs – potassium feldspar; Bt – biotite; Qz – quartz; Px – pyroxene; OM – opaque minerals; LC – lithic clasts; see Table S2 for WGS84 coordinates

The degree of anisotropy ( $P$ ) indicates the intensity of magnetic fabrics, and the shape parameter ( $T$ ) defines the shape of the AMS ellipsoid (see details in the Supplementary information Text S1).

A total of 1359 right-cylinder specimens were collected at 68 sampling sites (~20 specimens per site). In addition, 26 representative thin-sections were examined with an optical polarizing microscope to study the rock petrography with emphasis on dominant susceptibility-bearing minerals (e.g., biotite, hornblende, pyroxene, and Fe-Ti oxides). Thermomagnetic measurements (N=12 representative specimens), hysteresis loops (N=9), and first-order reversal curve distributions (FORC; N=9) were obtained to aid with identifying the magnetic mineralogy. The methodology used in this paper follows the same protocol as described in Žák et al. (2021); the detailed methodology, statistical evaluation using the Jelínek methods (Jelínek and Kropáček 1978), and full dataset are provided in the Text S1 and Tab. S2. Representative results are shown in Figs. 4–8 and Figs. S3–S4.

## 4 Results

### 4.1 Bulk susceptibility

The variation of the  $k_m$  of all individual TR specimens scatters from 30 to  $6971 \times 10^{-6}$  (SI units; Tab. S2). Here, we informally distinguish paramagnetic ( $<500 \times 10^{-6}$ ), moderately ferromagnetic ( $500\text{--}2500 \times 10^{-6}$ ), and strongly ferromagnetic ( $>2500 \times 10^{-6}$ ) groups. The  $k_m$  of the Teichweg (N=169 individual specimens) is evenly distributed between  $35$  and  $465 \times 10^{-6}$  (Fig. 4a). For the Lugstein-Pramenáč (N=270), the  $k_m$  varies from 83 to  $3650 \times 10^{-6}$  SI; 38% of specimens are paramagnetic, 46% moderately ferromagnetic, and 16% strongly ferromagnetic. The Vlčí kámen (N=500) yields a wide spectrum of  $k_m$   $59\text{--}3096 \times 10^{-6}$ , yet paramagnetic values (62%) dominate over the moderately ferromagnetic (32 %) and the strongly ferromagnetic values (6 %; Fig. 4a). The  $k_m$  of the Přední Cínovec (N=358) indicates the widest range of values among the TR members from  $40$  to  $6971 \times 10^{-6}$ ; paramagnetic, moderately ferromagnetic, and strongly ferromagnetic values yielded 25%, 34%, and 41%, respectively. The Medvědí vrch (N=62) yields only paramagnetic susceptibility values with two main peaks between  $50\text{--}100 \times 10^{-6}$  and  $200\text{--}300 \times 10^{-6}$  (Fig. 4a).

## 4.2 Thermomagnetic curves

Two trends in the thermomagnetic curve behavior are distinguished. (1) Curves of the Teichweg yield a hyperbolic decrease of  $k_m$  from the liquid nitrogen temperature ( $-196\text{ }^\circ\text{C}$ ) to  $\sim 300\text{--}400\text{ }^\circ\text{C}$ . (Fig. 4b). This corresponds to paramagnetic behavior, which is inversely proportional to the absolute temperature according to the Curie–Weiss law (Levy 1968). This trend is followed by a slight decrease of  $k_m$  (samples FT001I, FT003, and FT105T), while the sample FT024 shows a slight increase of  $k_m$  with an abrupt drop of  $k_m$  marking a Curie temperature ( $T_c$ ) at  $\sim 560\text{ }^\circ\text{C}$  (Fig. 4b). The curves FT003 and FT105T are fully reversible, whereas samples FT001I and FT024 indicate elevated  $k_m$  on cooling curves. Such behavior corresponds to the formation of new Fe-Ti oxide phase(s) during the heating (Fig. 4b).

(2) Eight thermomagnetic curves of the remaining members have a prominent Verwey transition ( $V_t$ ; Verwey and Haayman 1941) between  $-162\text{ }^\circ\text{C}$  and  $-149\text{ }^\circ\text{C}$ . The  $k_m$  follows a slight hyperbolic decrease up to ca.  $-50\text{ }^\circ\text{C}$  (Fig. 4b). The  $k_m$  then defines a plateau on further heating with a pronounced peak (‘bump’) at  $\sim 280\text{ }^\circ\text{C}$ , in the case of samples PV004, PV017, and PV020. This pattern is followed by an abrupt  $k_m$  drop with a  $T_c$  between  $\sim 560\text{--}570\text{ }^\circ\text{C}$ . Another minor  $T_c$  is recorded at  $\sim 620\text{ }^\circ\text{C}$  and  $\sim 680\text{ }^\circ\text{C}$ . The remaining curves yield a flat pattern until they reach their  $T_c$  at  $\sim 560\text{--}570\text{ }^\circ\text{C}$  (Fig. 4b). On most cooling curves, the  $T_c$  and  $V_t$  are similar to those on the heating curves, but the  $k_m$  notably increases, and the pronounced ‘bumps’ at  $\sim 280\text{--}290\text{ }^\circ\text{C}$  are absent. The origin of the ‘bump’ on the heating curve and its absence on the cooling curve is not well understood. This behavior has been observed (1) in hydrothermally altered volcanic rocks (Ade-Hall et al. 1971; Gee et al. 2010); (2) in coarse-grained thermally metastable maghemite, for instance the inversion of maghemite (gamma- $\text{Fe}_2\text{O}_3$ ) to hematite (alpha- $\text{Fe}_2\text{O}_3$ ; Dunlop and Özdemir 1997); and (3) in pyrrhotite (Rochette et al. 1990). In the latter two cases, heating leads to a reordering and/or alteration of the material to a less magnetic phase leading to the absence of the ‘bump’ on the cooling curve. In our data, however, we observe an increase in the susceptibility on the cooling curve. These changes suggest alteration of specific Fe-Ti oxide phase(s) and the growth of new Fe-Ti ferromagnetic oxide phase(s) with higher  $k_m$  following heating (Fig. 4b). Although the origin of the increase of susceptibility following heating remains topic for further study.

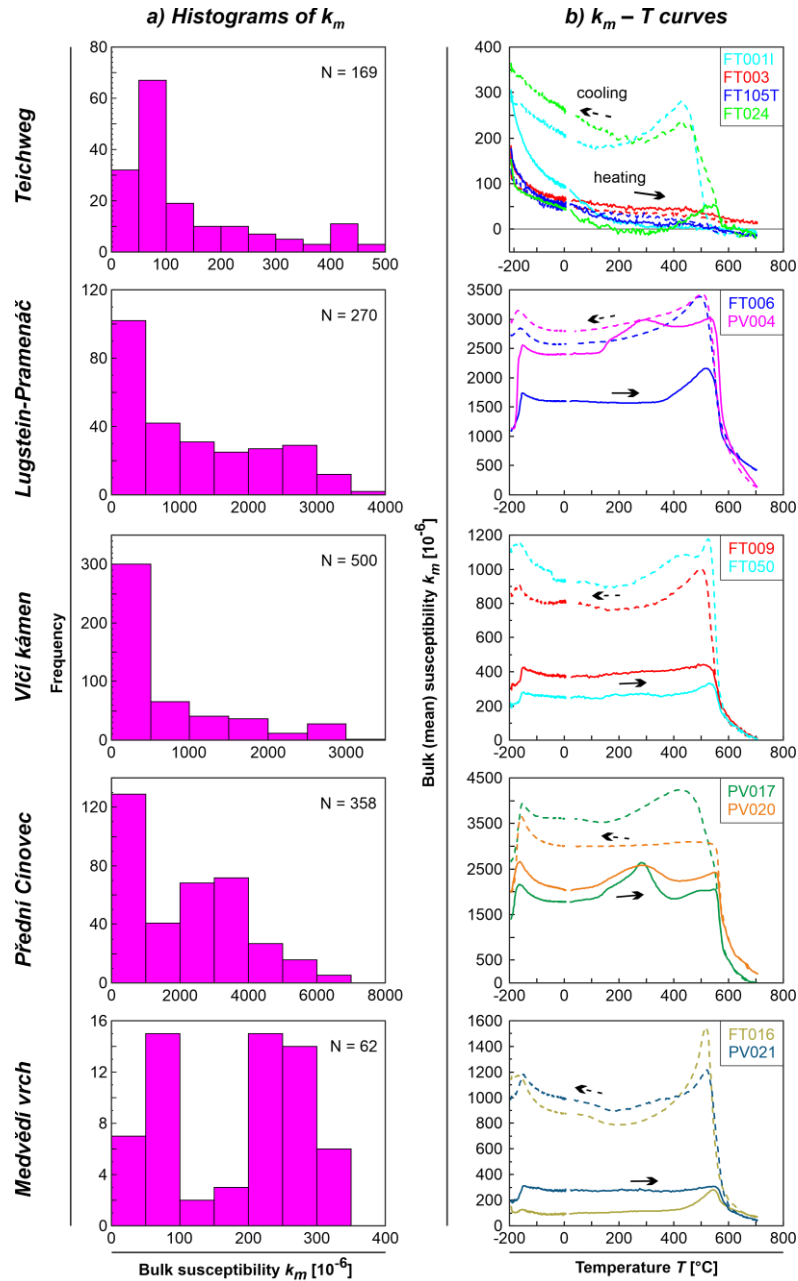


**Figure 4** Rock-magnetic data from the TR: a) histograms of bulk susceptibility; b) thermomagnetic curves showing bulk susceptibility vs. temperature dependence; see the text for details

#### 4.3 Hysteresis loops and FORCs

Four samples (FT003, FT019, FT105T, FT105I) yield a linear relationship between applied field and resulting magnetization intensity and lack hysteresis behavior. The other five samples (PV004, PV017, FT006, FT009, PV020) yield hysteresis loops characterized by steep acquisition reaching saturation between 0.42 T to 0.60 T applied fields (Figs. 5a and S3). The mass-normalized saturation magnetization values vary from  $1.24 \times 10^4 \text{ Am}^2/\text{kg}$  to  $25.7 \times 10^4 \text{ Am}^2/\text{kg}$  with an average saturation magnetization of  $7.16 \times 10^4 \text{ Am}^2/\text{kg} \pm 6.51 \times 10^4$

$\text{Am}^2/\text{kg}$  at  $1\sigma$ . Sample FT009 yields a slightly different hysteresis behavior characterized by a moderately wasp-waisted curve shape (Fig. 5a). Such curves indicate a mixture of magnetic material with different coercivity fractions. A mixture of single-domain (SD)/superparamagnetic (SP) can produce wasp-waisted loops (Roberts et al. 1995) as well as mixtures of two minerals, one magnetically soft and one magnetically hard (Carvallo et al. 2006).

FORC distributions provide a rapid means for examining the magnetic domain state or states present within the sample (Roberts et al. 2000). The FORC distribution for an SD grain is highly peaked on the  $H_u = 0$  axis and the contours elongated with negligible vertical spread. The distributions of the larger multi-domain (MD) grains display no peak and plot close or on the Y-axis (Text S1). Of the five samples that show ferromagnetic hysteresis behavior (PV004, PV017, PV020, FT006, FT009), sites PV020, FT006, and FT009 yield FORC distributions indicative of MD grains. Sites PV004 and PV017 show a slight elongation along the X-axis that we tentatively interpret to reflect a mixture of domain states within the materials (Figs. 5b and S3).

#### 4.4 Degree of anisotropy and shape parameter

The degree of anisotropy varies between 1.001 and 1.065 (0.1–6.5% of anisotropy), and the shape parameter ranges from  $-0.97$  to  $0.92$  (prolate to oblate) for all TR individual specimens (Tab. S2). In this paper, we distinguish prolate ellipsoids for  $T$  from  $-1$  to  $-0.1$ , neutral ellipsoids with  $T$  from  $-0.09$  to  $0.09$ , and oblate for  $T$  from  $0.1$  to  $1$ . In the Teichweg, the site-mean  $P$  yields 0.7–2.4%, and the site-mean  $T$  ranges between  $-0.27$  and  $0.59$ . All ignimbrite sites and one ash-fall tuff site are oblate in shape, whereas another ash-fall tuff site is prolate (Fig. 6a and b). The Lugstein-Pramenáč has a  $P$  of 1.0–3.6% and  $T$  between  $-0.35$  and  $0.29$  (38% of AMS sites are prolate, 31% neutral, and 31% oblate in shape). The Vlčí kámen is characterized by 0.4–2.5% of anisotropy, and the  $T$  value ranges between  $-0.25$  to  $0.70$  (25% prolate, 16% neutral, and 58% oblate). The Přední Cínovec yields  $P$  in the range of 1–3.2%, while  $T$  varies from  $-0.53$  to  $0.36$  (53% prolate, 26% neutral, and 21% oblate). The Medvědí vrch indicates 0.8–2.1% of anisotropy and a spread of  $T$  values from  $-0.47$  to  $0.21$  (20% prolate, 60% neutral, and 20% oblate; Fig. 6a and b).

In map view, a general spatial distribution of  $P$  and  $T$  parameters occurs across the sampling region. The Teichweg yield oblate-shaped ellipsoids with a lower  $P$  (Fig. 7a and b). The AMS fabrics with a higher  $P$  cluster in the central portions of the Lugstein-Pramenáč and

Přední Cínovec, while their margins are dominated by the weakly anisotropic samples of neutral and oblate AMS ellipsoids (Fig. 7a and b). The Vlčí kámen shows overall oblate fabrics in the southern and northern portions with the central narrow belt dominated by prolate fabrics; both domains are characterized by a weak P. Given the low distribution of sampling sites, the Medvědí vrch does not show any obvious spatial trends (Fig. 7a and b).

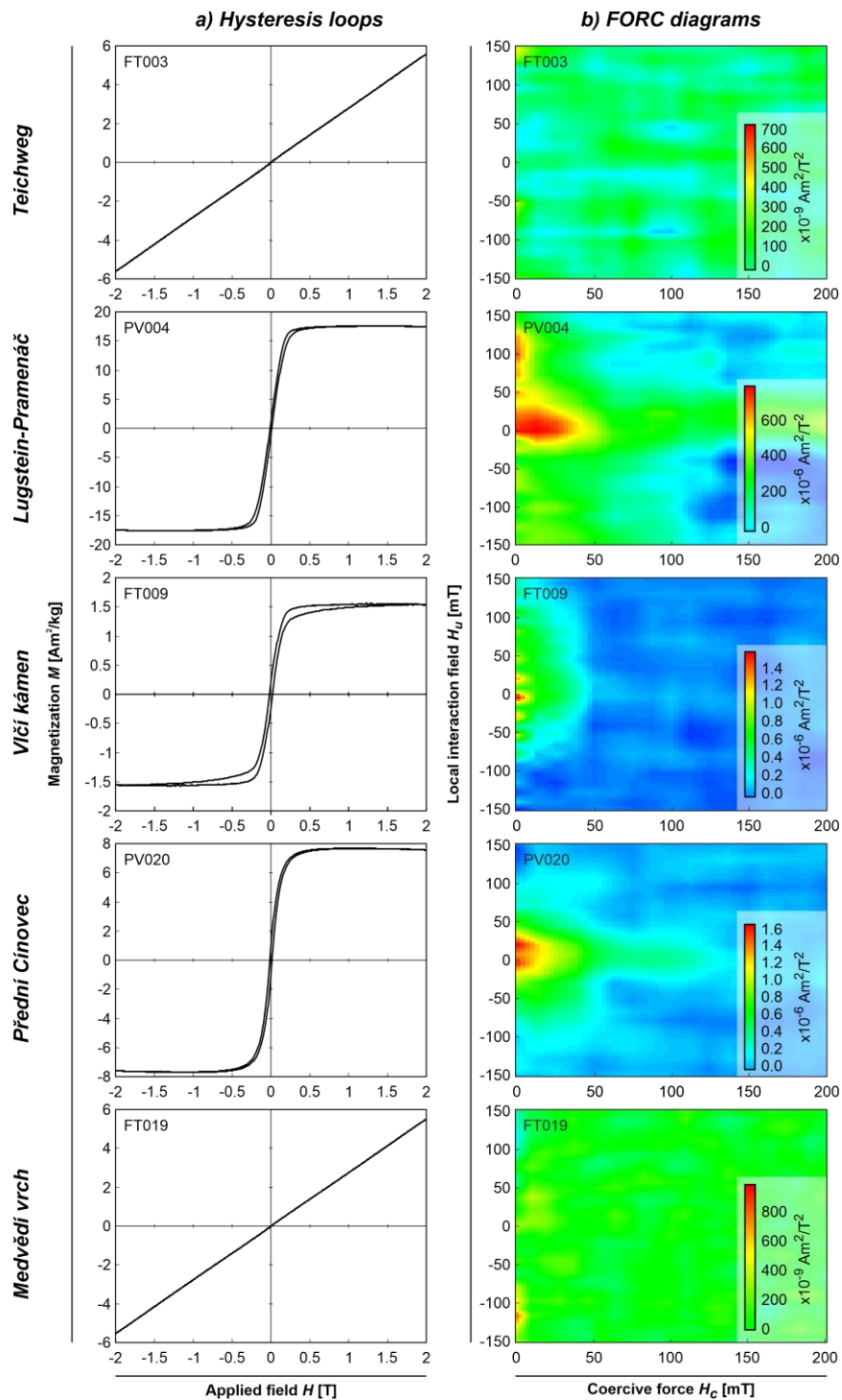


**Figure 5** Rock-magnetic data from the TR: a) hysteresis loops; b) FORC diagrams; see the text for details

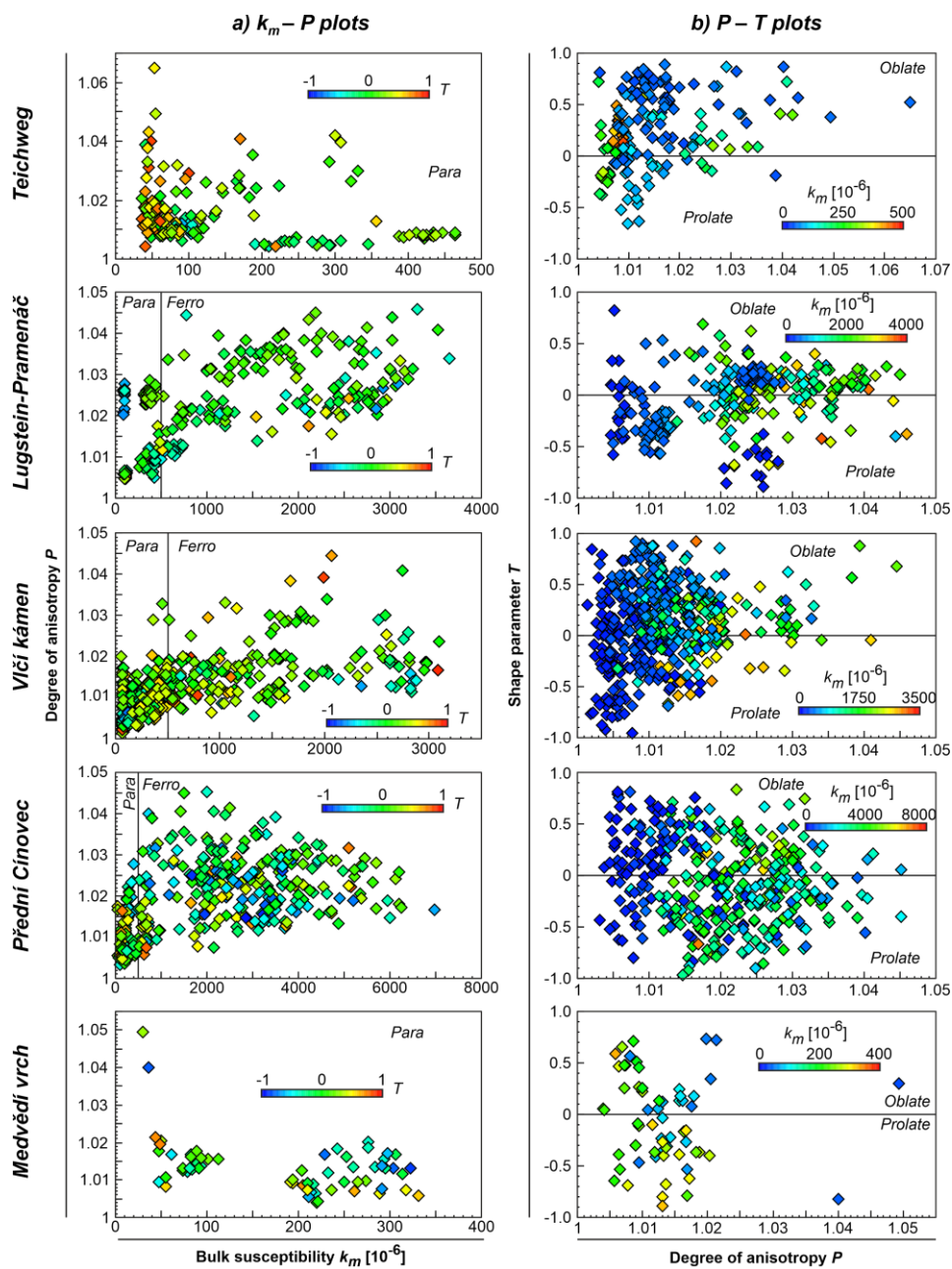


**Figure 6** AMS parameters from the TR: a)  $k_m - P$  plots; b)  $P - T$  plots; para – paramagnetic; ferro – ferromagnetic; see the text for details

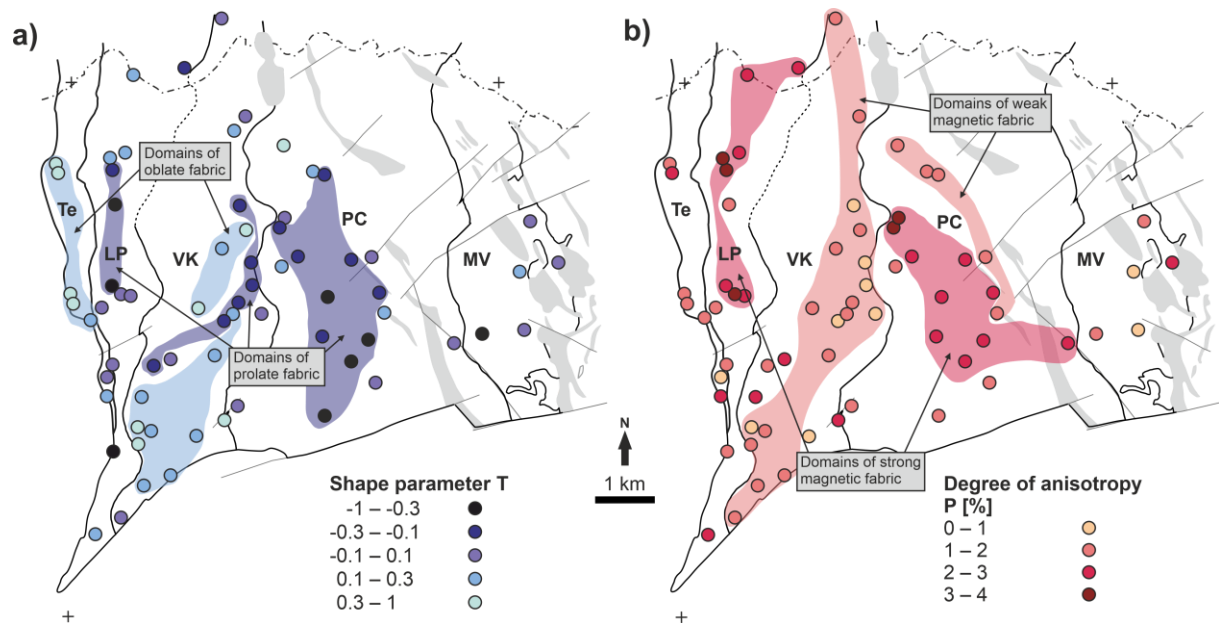


**Figure 7** Simplified maps depicting spatial trends of site mean a) shape parameter and b) degree of anisotropy; maps are based on Figure 2a

#### 4.5 Orientations of magnetic fabrics

##### 4.5.1 Data processing

Given the generally eastward trapdoor tilt of the caldera, all the AMS directional data were first reoriented back to the pre-collapse position to constrain the original flow directions. The trap-door collapse occurred after the emplacement of the most voluminous Přední Cínovec ignimbrite (Tomek et al. 2019, 2022). As such, the collapse was synchronous with the emplacement of the ring dike system (Fig. 1a–c), which in many places occurs along the caldera periphery where they intrude the older TR ignimbrites.

The trap-door collapse style of the ATC was first recognized by Benek (1991), who examined 78 drillholes in the German part, from which 34 drill holes pierced through the basement of the TR. Based on these data, Benek (1991) estimated the DRE volume of the TR (100–120 km<sup>3</sup>, now recalculated to total of 350 km<sup>3</sup>; Tomek et al. 2022) on the German side, but also revealed the trapdoor tilt that shallowly dips roughly to the east-southeast. Similarly, based on observations in mine shafts (now closed) on the Czech side of the ATC, Jiránek et al. (1987) approximated that the tilted trap-door floor dips 20–40° roughly towards the east and east-northeast. Schovánek et al. (2004) reported that basal contact of the crystalline basement dips ‘under’ (towards the east-northeast) the Teichweg and Lugstein-Pramenáč ignimbrites at angles up to 45°. Lastly, Fiala (1959) described that the Teichweg and Lugstein-Pramenáč



ignimbrites along the western margin of the present-day exposure of the TR dip ‘shallowly’ (angle not specified) towards the east-northeast. The volcanoclastic, siliciclastic, and charcoal layers intercalated within some of the TR ignimbrites are preserved only in boreholes (Eisenreich and Jeřábek 1978; Breiter et al. 2001). Two ash-fall tuff layers exposed in outcrops in the German part of the ATC are located in areas affected by intense faulting (Lobin 1986). Thus, the data from the intercalated volcanic and sedimentary layers are not reliable indicators of dip direction and dip of the caldera floor.

In addition, we have measured the bedding of the Teichweg ash-fall tuff at the base of the Teichweg ignimbrite (Fig. 3). The calculated mean dip direction and dip are  $068^\circ$  and  $27^\circ$ , respectively. These data are consistent with previously documented east-northeastward  $20^\circ$  to  $40^\circ$  dip of the contact between the crystalline basement of the caldera floor and overlying TR ignimbrites.

The calculated mean orientation was input into the AGICO ANISOFT 5 software to recalculate the original paleohorizontal orientation of AMS and flow fabrics of the TR ignimbrites on top of the Teichweg ash-fall tuff. Following this structural correction, further data analysis of particle imbrication during emplacement and depositional processes of PDC can be accomplished (Fig. 8a).

#### 4.5.2 Data description

The Teichweg ignimbrite flow foliation is defined by the shape preferred fiamme orientation measured in the field (Fig. 8b). After correcting for the structural tilt about a horizontal rotational axis, the foliation dips shallowly to the east with a mean value of  $092^\circ/14^\circ$ . The AMS fabrics of the Teichweg ignimbrite show well-clustered  $k_1$ ,  $k_2$ , and  $k_3$  axes of individual specimens around their mean orientation at most outcrops, although some sites display subhorizontal girdles of  $k_1$  and  $k_2$  axes, and a well clustered  $k_3$  axes (Figs. 8b and S4). The magnetic foliations dip at a maximum angle of  $35^\circ$ , generally both the east and west. However, some sites also show dip directions of magnetic foliations to the southeast and south (Figs. 8b, and S4).

The magnetic fabrics of the Lugstein-Pramenáč, Vlčí kámen, and Přední Cínovec show well-clustered principal susceptibility axes from the individual specimens around their mean direction. Six sites (i.e. FT032) yield poorly clustered principal susceptibility axes. These sites are interpreted with great caution (Figs. 8c-e, 9d, and S4). Sites FT027 and FT040

showed very poor clustering of susceptibility axes and were excluded from flow direction estimates (Figs. 8 and S4).

The dominant magnetic foliations of the Lugstein-Pramenáč ignimbrites dip at a maximum angle of  $40^\circ$ , however, some sites yield a steeper to subvertical attitudes. With a few exceptions, most of the foliations dip to the east-southeast, whereas at some sites south and west-dipping foliations were measured (Figs. 8c and S4). The associated magnetic lineations are generally shallow with a maximum plunge value of  $41^\circ$ . The northern portion reveals a generally eastward trend, whereas in the southern portion the lineations plunge either towards north or south (Figs. 8c and S4).

The magnetic foliations from the Vlčí kámen dip, in general, at steep angles with six sites having a maximum dip of  $50^\circ$ , 12 sites have a maximum dip of  $70^\circ$ , and six sites have dips between  $70$  and  $90^\circ$ . Most of the foliations dip to the east, east-southeast, and southeast, whereas at some sites, the foliation dip to the west-northwest, northwest, south-southwest, and south (Figs. 8d and S4). The associated magnetic lineations have various trends across the exposed area, with a maximum plunge of  $44^\circ$ , while at three sites the lineations plunge  $54^\circ$  (PV011),  $58^\circ$  (FT157), and  $66^\circ$  (FT042; Figs. 8d and S4, Tab S2).

The magnetic foliations of the Přední Cínovec ignimbrites are somewhat different; they are dominantly steep to subvertical, although at several sites the foliations dip moderately to subhorizontally. With a few exceptions, most of the magnetic foliations dip either to the south-southeast and southeast or to the northwest. The associated magnetic lineations are generally subhorizontal plunging either to the southwest or to the northeast. A few rare exceptions to this trend are steep to subvertical lineations, at two sites (Figs. 8e and S4). The fabric pattern thus defines a girdle of  $k_3$  axes ( $\pi$  plane  $040^\circ/69^\circ$  and girdle axis  $220^\circ/21^\circ$ ) while the mean magnetic lineation calculated from all individual specimens of the Přední Cínovec ( $219^\circ/09^\circ$ ) represents the girdle axis (Fig. 8e).

No significant spatial trends of magnetic fabrics of the Medvědí vrch were observed. The traces of steep magnetic foliations tend to wrap around adjacent post-caldera intrusions, while the associated lineations vary greatly from subvertical down-dip to subhorizontal along strike of foliations (Fig. 8f). In addition, no spatial dependence of  $k_m$ ,  $P$ , and  $T$  parameters on magnetic fabrics was found across the studied area (Figs. 7a, b, and S4, Tab. S2).

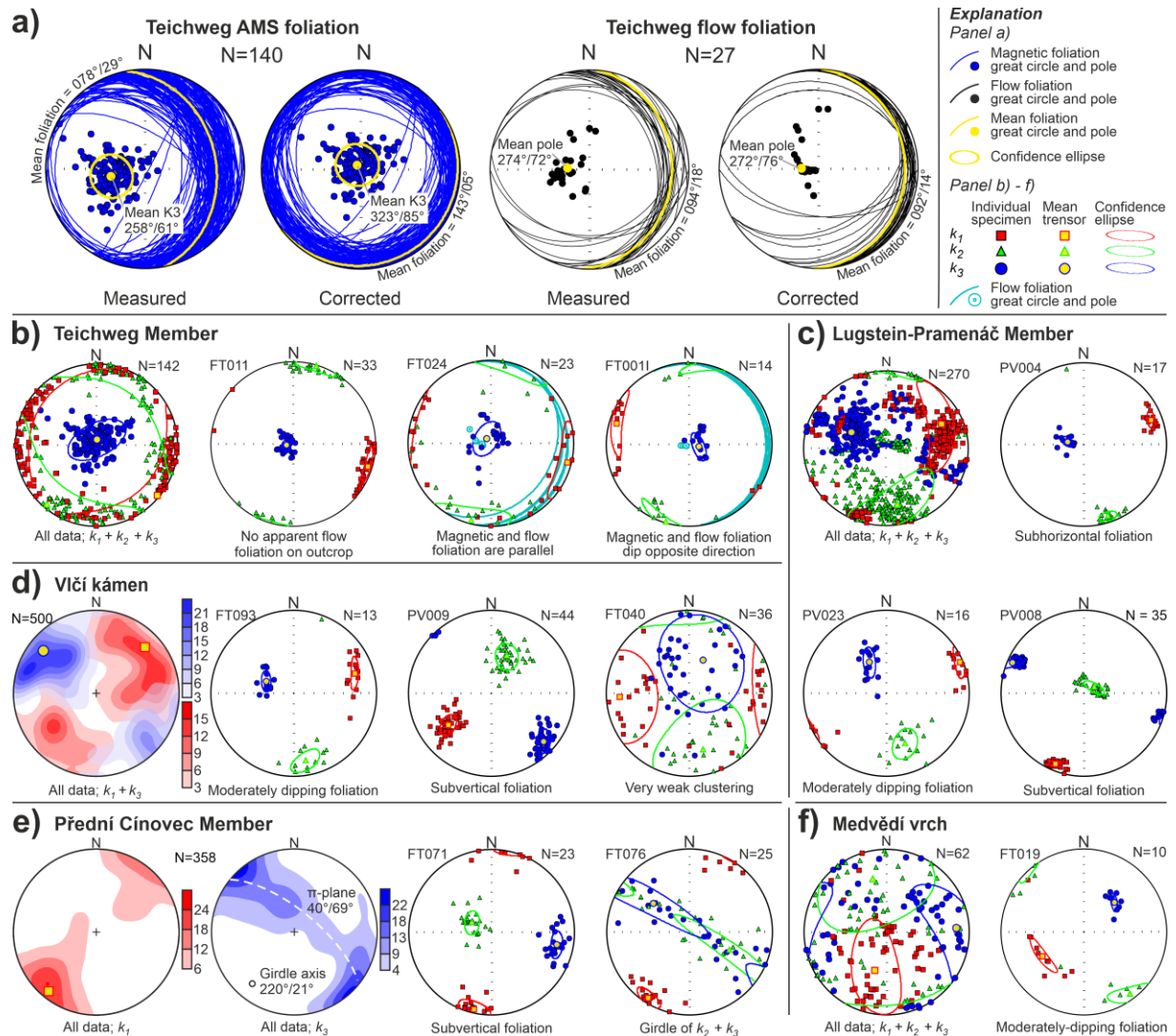


**Figure 8** Equal-area, lower hemisphere stereographic projections: a) comparison of measured and tilt-corrected structural data of magnetic and flow foliations, see the text for details; b-f) examples of typical magnetic fabrics of TR; Kamb contours are standard deviations

## 5 Discussion

### 5.1 Source of AMS signal

As evidenced by low  $k_m$  values, FORC distributions, thermomagnetic, and hysteresis curves, the magnetic fabrics of the Teichweg Member are controlled by paramagnetic phase(s), likely Fe-Mg silicates including biotite. The possibility of the presence of an inverse fabric related to SD ferromagnetic grains or certain mineral phases (e.g., tourmaline or monoclinic amphibole) is highly unlikely (e.g., Černý et al. 2020).

The high  $k_m$  values, Verwey transitions, and Curie temperature of  $\sim 560$ – $570$  °C in the Lugstein-Pramenáč, Vlčí kámen, and Přední Cínovec suggest that low-Ti titanomagnetite is the principal carrier of the AMS signal. Minor  $T_c$  at  $\sim 620$  °C and  $\sim 680$  °C (Fig. 4b) imply a

slight contribution of fine-grained high-Ti titanomagnetite and titanohematite. Lower susceptibility cooling curves following the heating curves with elevated ‘bumps’ of  $k_m$  at ~280–290 °C do not support the presence of maghemite or pyrrhotite. In addition, as we noted above, the  $k_m$  ‘bump’ at ~280–290 °C may reflect a type of hydrothermal alteration of the magnetic phase(s) in the sample, leading to the creation of magnetic phase(s) with a higher  $k_m$  following the heating. The FORC distributions and hysteresis curves indicate that the dominant domain state is MD in all analyzed specimens in Lugstein-Pramenáč, Vlčí kámen, and Přední Cínovec with a possible minor contribution of SP and SD grains. The AMS fabrics reflect the shape anisotropy of the MD low-Ti titanomagnetite grains (Fig. 3f–h). The contribution from distribution anisotropy (grain-to-grain magnetic interactions) and SD and SP grains to the AMS fabrics is negligible (Potter and Stephenson 1988; Hargraves et al. 1991; Rochette et al. 1992, 1999; Stephenson 1994; Grégoire et al. 1995, 1998; Cañón-Tapia 1996; Harrison and Feinberg 2008).

The thermomagnetic curves of the Medvědí vrch indicate a mixed paramagnetic and ferromagnetic signal. However, the low  $k_m$  values, hysteresis loops, and FORC distributions reflect a nearly pure paramagnetic behavior (Figs. 4a, b, 5a, and b). We interpret that the AMS signal of the Medvědí vrch is dominated by paramagnetic Fe-Mg silicates with a possible minor contribution of a ferromagnetic phase. The difference in the magnetic mineralogy of Vlčí kámen and Medvědí vrch indicates that these ignimbrites likely represent different erupted magmas as compared to the conclusion of Casas-García et al. (2019) who interpreted them as one lithostratigraphic member.

## 5.2 PDC flow directions and post-emplacement processes

The magnetic fabrics in the ignimbrite studies are classified into three groups based on the acute angle between magnetic foliation dip direction and the magnetic lineation trend: (1) normal 0–35°; (2) oblique 35–55°; and (3) transverse > 55° (Agrò et al. 2015). The PDC flow directions are determined from the  $k_3$  axis direction (flow direction arrows in Figs. 9a and 10), which corresponds to the fabric imbrication with respect to the basal flow plane of the deposit (e.g., Fisher et al. 1993; Le Pennec et al. 1998; Giordano et al. 2008; LaBerge et al. 2009; Cas et al. 2011; Gountié Dedzo et al. 2011; Lerner et al. 2022). In previous studies, the shape of the AMS ellipsoids from ignimbrites is, in most cases, oblate (e.g., Ellwood 1982; Knight et al. 1986; Agrò et al. 2015; Ort et al. 2015; Moncinhatto et al. 2019). A normal fabric has a magnetic lineation parallel or near parallel to the flow direction. Numerous studies have

argued that a normal magnetic fabric represents a laminar PDC flow regime (MacDonald and Palmer 1990; Baer et al. 1997; Ort et al. 1999, 2003, 2015; Haag et al. 2021). An oblique and transverse fabric yields a lineation at a high angle and perpendicular to the flow direction, respectively. The transverse fabrics are consistent with the effect of turbulent bed-load rolling of the magnetic grains that orients the long axis of the grains perpendicular to flow direction (Ort et al. 1999; Baas et al. 2007). The oblique fabric may represent a transition between a normal and a transverse magnetic fabric (Agrò et al. 2015).

On the other hand, steeply dipping magnetic foliations and prolate AMS ellipsoids are less abundant in ignimbrite deposits. They may originate through a combination of several factors: (1) ductile tectonic overprint; (2) changes in flow dynamics due to the interaction of flow with other flow pulses, basal obstacles, and/or lateral barriers; (3) variations or alteration of magnetic mineralogy, and (4) high degree of welding compaction and/or rheomorphic viscous flow, shearing, and folding (Ellwood 1982; Lamarche and Froggatt 1993; Borradaile and Werner 1994; Le Pennec et al. 1998; Wang et al. 2001; Martín-Hernández and Hirt 2003; Pioli et al. 2008; Geissman et al. 2010).

#### *5.2.1 Teichweg Member*

The PDC flow direction that deposited the Teichweg ignimbrites are interpreted based on the following criteria. (1) The flow directions are inferred from the imbrication of flattened fiamme and paramagnetic minerals with respect to the basal flow plane (i.e., the ash-fall tuff bedding; see section 4.5.1). The PDC flow direction corresponds to the trend of the pole/normal to the shallowly dipping foliation plane (a maximum dip of 35°). (2) The dominance of oblate-shaped and normal fabrics characterizes a laminar PDC flow regime (71% sites with normal and 29% with transverse fabrics; Figs. 9b and 10). (3) The low degree of anisotropy (0.7–2.4%) excludes a ductile tectonic overprint.

On most sites, the east and east-southeast dipping magnetic foliations are generally parallel with the flow foliation defined by the shape-preferred orientation flattened fiamme (Figs. 8a and S4). The fiamme developed during deposition, post-emplacement loading compaction, and moderate-degree of welding from a pumice-rich PDC (e.g., Walker 1983; Druitt 1998; Branney and Kokelaar 1992; Casas García et al. 2019). The poles/normals to both foliation planes thus indicate that the general direction of the PDC route is from the east (east-southeast) to the west (west-northwest). In a few cases, where the flow and magnetic foliations yielded opposite orientation, the pole to the east-dipping flow foliation was used to

estimate the PDC transport direction (Figs. 8b and 9b). Such deviations likely reflect the interplay between paleotopography irregularities during ignimbrite deposition. The westward direction is further corroborated by the asymmetry of fiamme in flow foliation planes (Figs. 3c, 8b, 9b, 10, and S4).

### 5.2.2 *Lugstein-Pramenáč and Vlčí Kámen*

All the younger TR members lack macroscopic petrofabric markers as proxies for the magnetic fabric orientation. Therefore, we have to rely only on the AMS fabrics. At Lugstein-Pramenáč, 31% of sites exhibit normal, 23% oblique, and 46% transverse fabrics. The degree of anisotropy is slightly higher (1.0–3.6%), and the shape parameter is evenly distributed from prolate to oblate. At Vlčí kámen, 4% of the sites yield normal, 26% oblique, and 70% transverse fabrics. The degree of anisotropy ranges between 0.4% and 2.5%, while oblate fabrics dominate over neutral and prolate fabrics. The shape parameter varies spatially in both members with oblate fabrics along the contacts and prolate fabrics in the center of the deposits (Figs. 7a, b, 8c, 9c, and 10). Petrographic observations of Casas García et al. (2019) indicate a higher degree of welding as compared to the Teichweg member.

The zonal pattern of the spatial distribution of  $P$  and  $T$  parameters is consistent with the interpretations of Platzman et al. (2020), who found that a voluminous flow unit (up to ~1 km in thickness) may contain prolate-shaped and steep magnetic fabrics in the ignimbrite's hot core as compared to colder rim with oblate and shallow foliations. In the hot core of these voluminous ignimbrites, the steep foliations may have developed due to the high degree of welding and possible rheomorphic simple shear deformation superposed on the flow fabric. No evidence exists for regional ductile deformation in this area and no mineralogical or magnetic grain size factors explain these fabric orientations. A possible effect of paleotopography on the flow regime and fabric evolution cannot be ruled out, but we did not find evidence to support this hypothesis.

Similarly to the Teichweg Member, we interpret that the Lugstein-Pramenáč and Vlčí kámen ignimbrites were emplaced from generally westward to west-northwestward moving PDCs with a possible effect of topographic obstacles that may have locally influenced the flow fabric orientations (Figs. 10 and 11a–c).

### 5.2.3 Přední Cínovec

At Přední Cínovec, 22% of sites have normal, 6% oblique, and 72% transverse fabrics. The degree of anisotropy is 1.0–3.2% and the shape of AMS ellipsoids is dominantly neutral. The magnetic fabric pattern defines a girdle of normals to the foliation planes ( $k_3$ ) with a subhorizontal axis defined by the lineations ( $k_1$ ; Figs. 8e and 10), which is distinct compared to the other TR members. Such a pattern is consistent with folding deformation with a maximum shortening direction oriented NNW-SSE, and not with a PDC flow and depositional processes. In addition, similarly to the Lugstein-Pramenáč and Vlčí Kámen ignimbrites, the Přední Cínovec yields a zonal pattern of AMS parameters spatial distributions with prolate fabrics in the ignimbrite interiors surrounded by neutral and oblate shapes (Figs. 7a, b, and 10).

We interpret that most of the primary emplacement fabrics that record the PDC flow directions are obscured by a high-degree of welding, syn-emplacement simple shear ductile deformation, and progressive rheomorphic folding (Hargrove and Sheridan 1984; Branney and Kokelaar 1992; Branney et al. 1992; Kobberger and Schmincke 1999; Andrews and Branney, 2005; Geissman et al. 2010; Gambeta et al. 2021). As such, we may only speculate that the original flow directions were oriented in the NNW-SSE direction. During the emplacement of the most voluminous Přední Cínovec ignimbrite ( $\sim 70 \text{ km}^3$  DRE; Tomek et al. 2022), the caldera had already commenced subsiding in a piston style (Tomek et al. 2019). This caldera depression was rapidly filled by the hot ignimbrite from the NNW and SSE. With continuing subsidence and caldera eruptions depositing new pyroclastic material, the ignimbrite was progressively sheared and folded in a northwest-southeast direction (general vergence of inclined axial fold plane), which led to the formation of the fold pattern of the AMS fabric (Fig. 11d; e.g., Hargrove and Sheridan 1984; Geissman et al. 2010).

We may only speculate that the increasing proportion of transverse fabrics from the Lugstein-Pramenáč, through Vlčí kámen to Přední Cínovec ignimbrites may reflect the progressive intensification of welding and rheomorphic ductile deformation within the ignimbrite sequences. An underlying assumption in our interpretation is that the trend of magnetic lineation perpendicular to the magnetic foliation dip direction defines the development of a fold axis lineation. Hence, the lineation is perpendicular to the maximum shortening direction during rheomorphic folding.

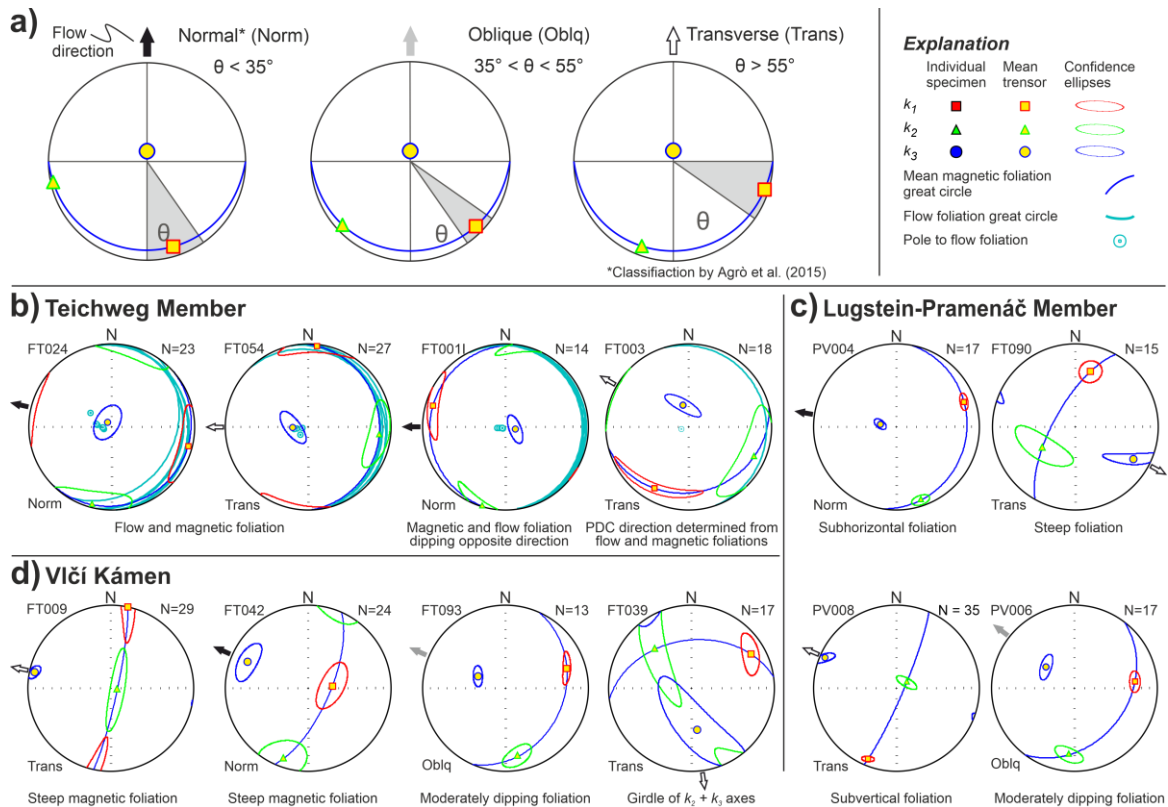


**Figure 9** Equal-area, lower hemisphere stereographic projections: a) classification of ignimbrite magnetic fabrics; b-d) examples of flow directions and classifications of Teichweg Member, Lugstein-Pramenáč Member, and Vlčí kámen ignimbrites

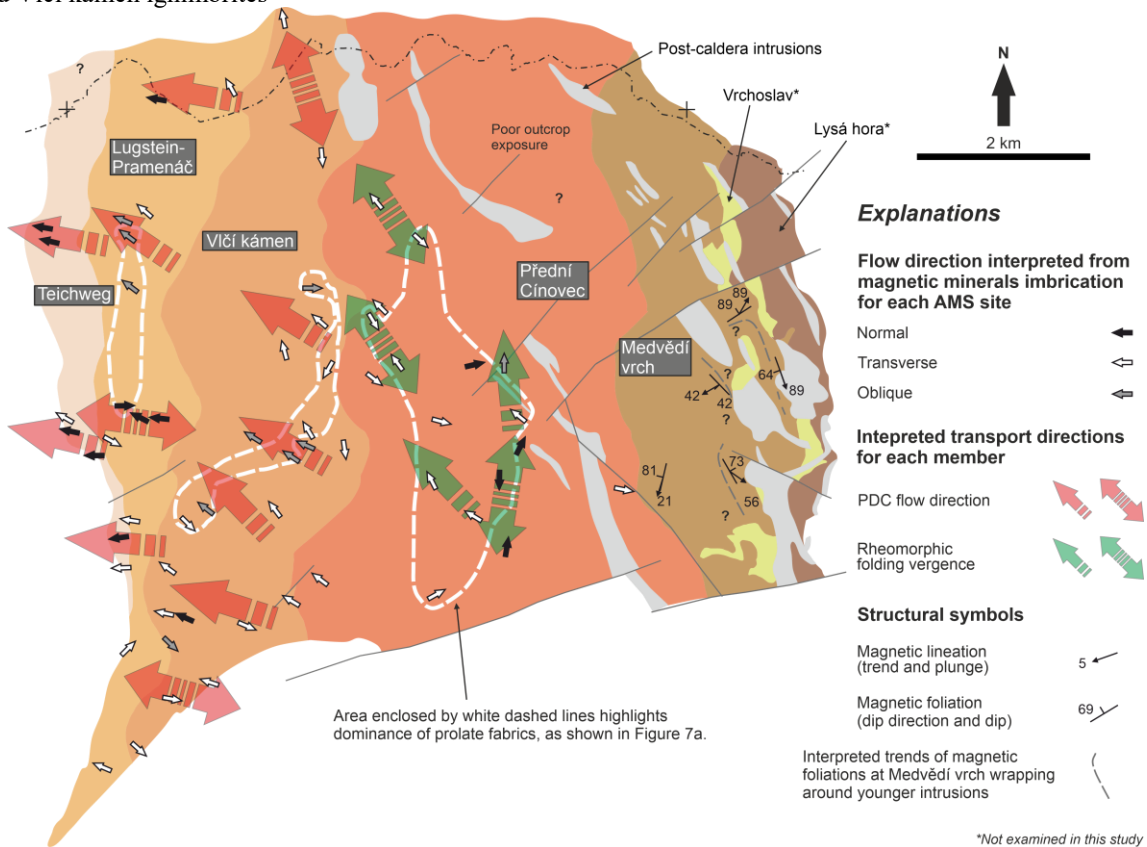


**Figure 10** Simplified map showing the interpreted flow directions at individual sampling sites and general flow trends; see the text for details; the map is based on Figure 2a



### 5.3 Source vent locations and caldera dynamics

The ignimbrites emplaced prior to caldera-forming eruption (Teichweg, Lugstein-Pramenáč, and Vlčí kámen) yield a dominantly west- to west-northwestward direction of PDC emplacement (Fig. 10). Some areas in the Lugstein-Pramenáč and Vlčí kámen, however, yield fabrics consistent with opposite flow directions, which may reflect either a paleovalley-induced backflow (Fisher et al. 1993; Ort et al. 2003; Gurioli et al. 2002, 2005; Willcock et al. 2015), or the presence of some minor volcanic vents in the central and western part of the caldera area (Figs. 10, 11b, and c). In terms of the latter, at both of these locations, numerous rhyolite and microgranite dikes intrude the ignimbrites. These could have served as possible feeder magma pathways (Fig. 1a). This places the main eruptive vents to the eastern rim of the present-day caldera (Fig. 11–c). A few sites in the Vlčí kámen yield flow directions toward the northwest (Figs. 10 and 11c). This northwest direction is parallel to the dominant fabric pattern of the Přední Cínovec Member and thus may indicate migration of eruptive centers (see below). Vent migration has been documented in several field cases (e.g., Van Den Bogaard and Schmincke 1984; Wilson and Hildreth 2000; Pfeiffer 2001; Druitt 2014).

The Přední Cínovec Member lacks convincing PDC flow markers as determined from the magnetic fabric. We hypothesize that the vent locations were located to the north-northwest, in the area of the Sayda-Berggießhübel rhyolite dike swarm (Figs. 1a and 11d). A similar concept suggested by Winter et al. (2008) was recently corroborated by the new radiometric dating of rhyolite dikes of  $314 \pm 4$  and  $313 \pm 3$  Ma (U-Pb on zircons; Tomek et al. 2022), which overlaps with the  $\sim 313.83$ – $313.41$  Ma age of major caldera-forming eruptions (U-Pb on zircons; Opluštil et al. 2016). In addition, at least two boreholes within the central area of the Přední Cínovec revealed lithic- and fiamme-rich portions in otherwise uniform lithic- and fiamme-poor ignimbrite. We thus pose that other localized vents distributed in the caldera interior may have existed and were buried by volcanic deposits of later eruptions (Fig. 11d).

The PDCs that deposited the Přední Cínovec also flowed for another  $\sim 40$  km south of the caldera center, where correlative, non-welded, extra-caldera rhyolite ignimbrites of the same age are exposed ( $314 \pm 3$  Ma and  $313.41 \pm 0.07$  Ma; U-Pb on zircons; Tomek et al. 2022 and Opluštil et al. 2016, respectively). Here, the co-ignimbrite ash-cloud sourced the Bělka tuff ( $\leq 313.83 \pm 0.23$  Ma, U-Pb on zircons; Opluštil et al. 2016), a regional stratigraphic marker, which is present elsewhere in the central and western Bohemian Carboniferous basins (Tomek et al. 2022). After the exhaustion of the underlying magma chamber, the final trap-

door caldera collapsed synchronously with the emplacement of the ring-dike system (Fig. 1a and 11e; Tomek et al. 2019).

#### 5.4 Caldera resurgence?

We speculate that the magnetic fabric pattern of the Medvědí vrch ignimbrite indicates a local magma resurgence within the caldera as evidenced by the traces of steep magnetic foliations that wrap around the younger intrusions (Fig. 10 and 11e). If so, the emplacement of these dikes and plutons must have occurred soon after emplacement of the TR when the ignimbrites were still hot and ductile enough to allow transposition of magnetic fabrics that were reoriented in the structural aureole (Figs. 10a and 11e).

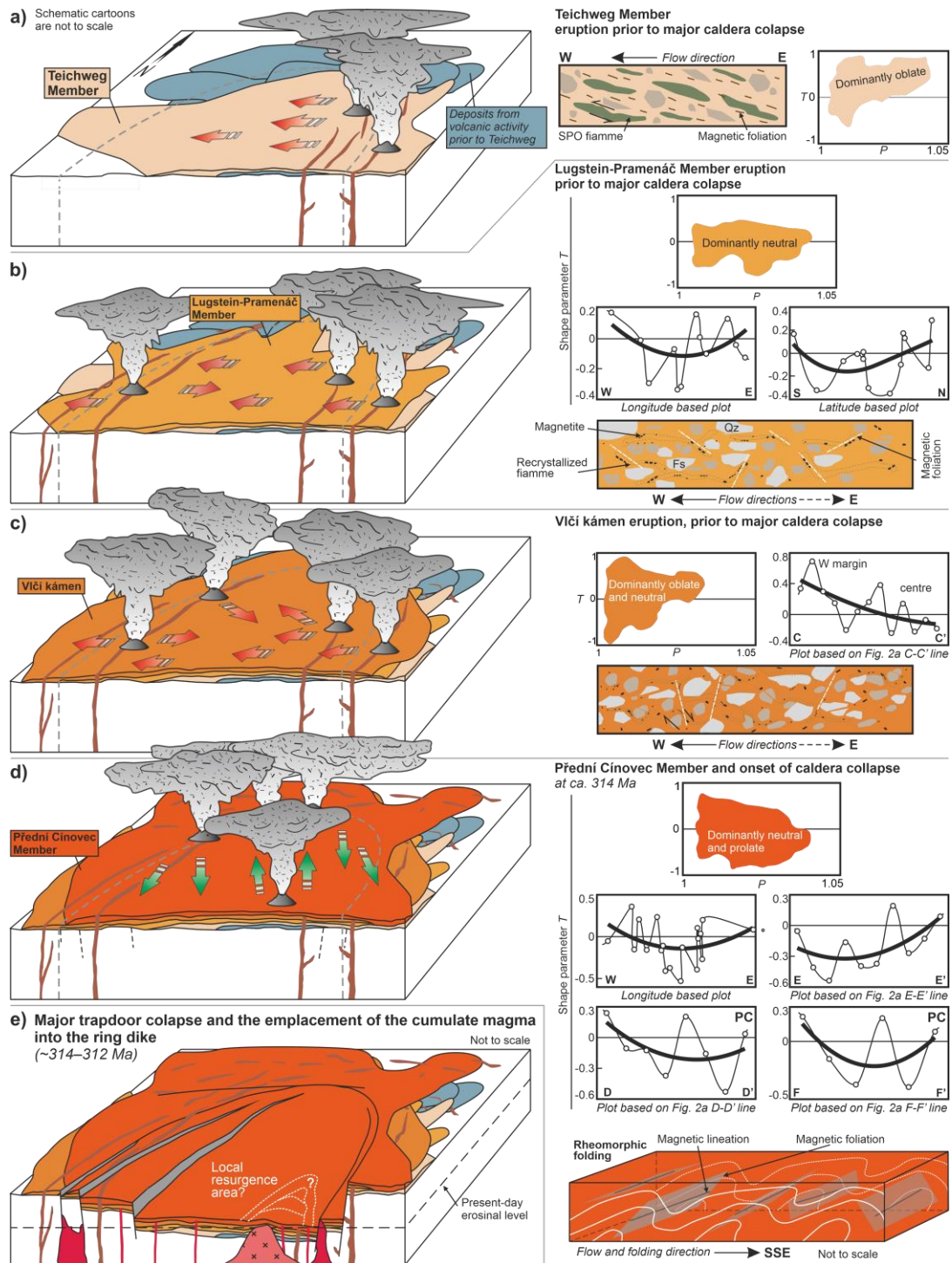


**Figure 11** Conceptual model showing the complex emplacement dynamics of examined TR members. The 3D cartoons (left section) illustrate the location of possible vent areas, eruption, flow directions and emplacement of (a) Teichweg, (b) Lugstein-Pramenáč, (c) Vlčí kámen, and (d) Přední Cínovec members. Panel (e) summarizes the final trap-door caldera collapse, ring dike, and granite emplacement associated with possible local resurgence along the eastern rim. The right section emphasizes our interpretations based on field and rock-magnetic data. The diagrams (labeled as ‘plots’) showing variations of shape parameter with location of sampling site (open symbol) were constructed along white lines shown in Figure 2a. The thick lines are second-degree polynomial regressive curves. The ‘Idealized cross-sections’ are based on either longitude or latitude data of AMS sample location. Interpretative kinematic cross-sections of magnetic fabric development during PDC flow and emplacement are shown for (a) Teichweg, (b) Lugstein-Pramenáč, and (c) Vlčí kámen ignimbrites. A three-dimensional model of transverse fabric development during rheomorphic folding is provided for (d) Přední Cínovec Member (see the text for details). Qz – quartz; Kfs – potassium feldspar; SPO – shape-preferred orientation. Color code of transport direction arrows corresponds to those in Figure 10.

## 5.5 General implications for magnetic fabric studies of high-grade ignimbrites

Our results from the TR ignimbrites are consistent with the fabric pattern of other moderately welded ignimbrites where the fabrics record stable sedimentation and imbrication of fiamme and mineral grains during PDC flow and emplacement (Giordano et al. 2008; Petronis and Geissman 2009; Cas et al. 2011; Agrò et al. 2015; Haag et al. 2021). On the other hand, the high-grade ignimbrites with neutral to prolate AMS ellipsoids and steep to subvertical magnetic foliations reflect fabrics affected by contemporaneous and/or secondary effects that influence the orientation of the fabric data. Some authors argued that such a pattern is complicated or even impossible to associate with the original flow directions of PDC (e.g., Wang et al. 2001; Gountié Dedzo et al. 2011; Pueyo Anchuela et al. 2014; Gambeta et al. 2021). In this study, however, field geologic evidence and detailed knowledge of the outcrop distributions across the field area allow for the PDC flow directions to be deduced. The underlying assumption is that the deposition and emplacement of the large volume ignimbrite (Přední Cínovec) were caused by a step-wise emplacement and welding compaction restricted to the initial piston caldera subsidence and superposed rheomorphic folding that transposed the primary fabric into the fold pattern. We conclude that in the case of intra-caldera high-grade ignimbrites, the flow and depositional processes, as well as the caldera dynamics, can be interpreted after careful data examination (e.g. Wilcock et al. 2015).

It is worth mentioning that the search for eruptive vent locations of such old, and possibly even older ignimbrites (e.g. Wilcock et al. 2015; Gambeta et al. 2021; this study) may lead to the identification of mineral ore deposits. For instance, as exemplified in the case of the ATC, one of the possible vent locations (borehole CIS-17; Figs. 2a and 3d) is closely related to the Cínovec pluton at the Czech/German border. This pluton hosts an extensive Sn-W-Li greisen deposit mined since 1378 CE (e.g. Breiter et al. 2019). Now both countries are conducting extensive prospection for Li resources as a response to global demand for the storage of electricity.

## 6 Conclusions

The magnetic fabric of the TR members reveals complex PDC dynamics from deposition, through welding and rheomorphic folding to possible caldera resurgence. The magnetic mineralogy revealed from the rock magnetic experiments of the TR ignimbrites indicates that the fabrics are carried by paramagnetic ferrosilicates (biotite and amphibole) in the Teichweg and Medvědí vrch members. The Lugstein-Pramenáč, Vlčí kámen, and Přední Cínovec

members yield a normal ferromagnetic fabrics dominated by MD low-Ti titanomagnetite. The small volume ignimbrites emplaced prior to caldera-formation yield dominantly westward to west-northwestward flow directions, which places the vent area along the eastern caldera rim. During the eruption of the Vlčí kámen, the vent areas likely migrated to the northwest. The main caldera-forming event erupted the high-grade ignimbrites of the Přední Cínovec. These ignimbrites underwent welding and rheomorphic deformation associated with ductile folding that obscured the primary flow fabrics. The previously published field evidence and radiometric data imply that Přední Cínovec ignimbrites were dominantly sourced from the northerly Sayda-Berggießhübel rhyolite dike swarm (~314 Ma). The draining of the underlying magma chamber triggered the final trap-door caldera collapse and emplacement of the ring dike system. The latter along with the intrusion of the post-caldera granites may have caused a local resurgence along the eastern caldera rim.

## Acknowledgment

The careful editorial handling by Mike Ort as well as the critical comments by Guido Giordano and an anonymous referee are highly appreciated. This manuscript is an integral part of the Ph.D. thesis of Petr Vitouš. We have benefited from discussions with Marion Tichomirowa, Bedřich Mlčoch, Marta Chlupáčová, Manuel Lapp, Jiří Žák, and Vladislav Rapprich. Milena Vostrá, Marta Tomková, and Jiří Petráček are thanked for laboratory assistance. State enterprises Czech forests (Lesy ČR) and Sachsen forests (Staatsbetrieb Sachsenforst) provided entrance and sampling permits on both sides of the border. Finally, we thank Geomet Ltd. for providing samples from their boreholes.

## Declarations

### Funding

This manuscript was supported by the Czech Science Foundation grant 19-02177Y (Tomek), Czech Academy of Sciences institutional support RVO67985831 (Vitouš, Tomek), and Charles University projects Cooperatio Programme (Research Area GEOL; Tomek), and Center for Geosphere Dynamics (UNCE/SCI/006; Vitouš, Tomek). Rock magnetic (hysteresis and FORC) analyses were supported by National Science Foundation grants DMR-1523611 and DMR-2122108 (PREM) awarded to Drs. T. Timofeeva and G. Gallegos at New Mexico

Highlands University. Petronis acknowledges the Fulbright program, which funded his visiting fellowship at Charles University.

Conflicts of interest/Competing interests

We declare no conflicts of interest or competing interests.

Availability of data and material

Datasets for this research are directly included in this paper, are available in the Supplementary information files, online through the Mendeley Data (<https://data.mendeley.com/datasets/yhn288f2rc/3>).

Code availability

Not applicable.

Ethics approval

Not applicable.

Consent to participate

Not applicable.

Consent for publication

Not applicable.

## References

- Ade-Hall JM, Palmer HC, Hubbard TP (1971) The magnetic and opaque petrological response of basalts to regional hydrothermal alteration. *Geophys J Int* 24:137-174.
- Agrò A, Zanella E, Le Pennec JL, Temel A (2015) Magnetic fabric of ignimbrites: a case study from the Central Anatolian Volcanic Province. *Geol Soc London Spec Publ* 396:159–175
- Andrews GDM, Branney MJ, (2005) Folds, fabrics, and kinematic criteria in rheomorphic ignimbrites of the Snake River Plain, Idaho: insights into emplacement and flow. *GSA Field Guide* 6:311–328
- Baas JH, Hailwood EA, McCaffrey WD, Kay M, Jones R (2007) Directional petrological characterisation of deep-marine sandstones using grain fabric and permeability anisotropy: methodologies, theory, application and suggestions for integration. *Earth-Sci Rev* 82:101–142
- Baer EM, Fisher RV, Fuller M, Valentine G (1997) Turbulent transport and deposition of the Ito pyroclastic flow: Determinations using anisotropy of magnetic susceptibility. *J Geophys Res Solid Earth* 102:22565–22586.
- Benek R (1991) Aspects of volume calculation of paleovolcanic eruptive products – the example of the Teplice rhyolite (east Germany). *Z Geol Wissenschaft* 19:379–389

- Borradaile GJ, Werner T (1994) Magnetic anisotropy of some phyllosilicates. *Tectonophysics* 235:223–248
- Branney MJ, Kokelaar P (1992) A reappraisal of ignimbrite emplacement: progressive aggradation and changes from particulate to non-particulate flow during emplacement of high-grade ignimbrite. *Bull Volcanol* 54:504–520
- Branney MJ, Kokelaar P (2002) Pyroclastic density currents and the sedimentation of ignimbrites. *Geol Soc London Mem* 27
- Branney MJ, Kokelaar BP, McConnell BJ (1992) The Bad Step Tuff: a lava-like rheomorphic ignimbrite in a calc-alkaline piecemeal caldera, English Lake District. *Bull Volcanol* 54:187–199
- Breiter K (2012) Nearly contemporaneous evolution of the A- and S-type fractionated granites in the Krušné hory/Erzgebirge Mts., Central Europe. *Lithos* 151:105–121
- Breiter K, Novák JK, Chlupáčová M (2001) Chemical evolution of volcanic rocks in the Altenberg-Teplice Caldera (Eastern Krušné hory Mts., Czech Republic, Germany). *Geolines* 13:17–22
- Breiter K, Hložková M, Korbelová Z, Galiová MV (2019) Diversity of lithium mica compositions in mineralized granite–greisen system: Cínovec Li-Sn-W deposit, Erzgebirge. *Ore Geol Rev* 106:12–27
- Cagnoli B, Tarling DH (1997) The reliability of anisotropy of magnetic susceptibility (AMS) data as flow direction indicators in friable base surge and ignimbrite deposits: Italian examples. *J Volcanol Geotherm Res* 75:309–320
- Cañón-Tapia E (1996) Single-grain versus distribution anisotropy: a simple three-dimensional model. *Phys Earth Planet Inter* 94:149–158
- Cañón-Tapia E, Mendoza-Borunda R (2014) Magnetic petrofabric of igneous rocks: lessons from pyroclastic density current deposits and obsidians. *J Volcanol Geotherm Res* 289:151–169
- Carvallo C, Muxworthy AR, Dunlop DJ (2006) First-order reversal curve (FORC) diagrams of magnetic mixtures: micromagnetic models and measurements. *Phys Earth Planet In* 154: 308–322
- Casas-García R, Rapprich V, Breitzkreuz C, Svojtka M, Lapp M, Stanek K, Hofman M, Linnemann U (2019) Lithofacies architecture, composition, and age of the Carboniferous Teplice Rhyolite (German–Czech border): insights into the evolution of the Altenberg-Teplice Caldera. *J Volcanol Geotherm Res* 386:106662. <https://doi.org/10.1016/j.jvolgeores.2019.106662>
- Černý J, Melichar R, Všianský D, Drahoukoupil J (2020) Magnetic anisotropy of rocks: a new classification of inverse magnetic fabrics to help geological interpretations. *J Geophys Res Solid Earth* 125:e2020JB020426. <https://doi.org/10.1029/2020JB020426>
- Chapin CE, Lowell GR (1979) Primary and secondary flow structures in ash-flow tuffs of the Gribbles Run paleovalley, central Colorado. *GSA Spec Pap* 180:137–154
- Druitt TH (1998) Pyroclastic density currents. *Geol Soc Spec Publ* 145:145–182.
- Druitt TH (2014) New insights into the initiation and venting of the Bronze-Age eruption of Santorini (Greece), from component analysis. *Bull Volcanol* 76:794. <https://doi.org/10.1007/s00445-014-0794-x>
- Druitt TH, Sparks RSJ (1984) On the formation of calderas during ignimbrite eruptions. *Nature* 310:679–681
- Dunlop DJ, and Özdemir Ö (1997) *Rock Magnetism: Fundamentals and Frontiers*. Cambridge University Press, New York
- Eisenreich M, Jeřábek M (1978) Geologic map of the Teplice rhyolite 1:10 000. *Czech Geol Surv*, Prague
- Ellwood BB (1982) Estimates of flow direction for calc-alkaline welded tuffs and paleomagnetic data reliability from anisotropy of magnetic susceptibility measurements: central San Juan Mountains, southwest Colorado. *Earth Planet Sci Lett* 59:303–314
- Fiala F (1960) The Teplice rhyolite between Krupka, Cínovec, Dubí and Mikulov and its surrounding rocks. *Bull Geosci* 26:445–494
- Fisher RV, Schmincke HU (1984) *Pyroclastic Rocks*. Springer, Berlin, Heidelberg
- Fisher RV, Orsi G, Ort M, Heiken G (1993) Mobility of a large-volume pyroclastic flow - emplacement of the Campanian ignimbrite, Italy. *J Volcanol Geotherm Res* 56:205–220
- Förster HJ, Tischendorf G, Trumbull RB, Gottesmann B (1999) Late-collisional granites in the Variscan Erzgebirge, Germany. *J Petrol* 40:1613–1645
- Gambeta JH, Savian JF, Sommer CA, Trindade RIF (2021) Magnetic anisotropy of an ancient volcanic system: Flow dynamics of post-collisional Ediacaran volcanism in southernmost Brazil. *Precambrian Res* 359:106209. <https://doi.org/10.1016/j.precamres.2021.106209>
- Gee JS, Yu Y, Bowles J (2010) Paleointensity estimates from ignimbrites: an evaluation of the Bishop Tuff, *Geochem Geophys Geosy* 11:Q0301. doi:10.1029/2009GC002834
- Geissman JW, Holm D, Harlan SS, Embree GF (2010) Rapid, high-temperature formation of large-scale rheomorphic structures in the 2.06 Ma Huckleberry Ridge Tuff, Idaho, USA. *Geology* 38:263–266
- Giordano G, Cas RAF (2021). Classification of ignimbrites and their eruptions. *Earth-Sci Rev*, 220, 103697. <https://doi.org/10.1016/j.earsci.2021.103697>
- Giordano G, Porreca M, Musacchio P, Mattei M (2008) The Holocene Secche di Lazzaro phreatomagmatic succession (Stromboli, Italy): evidence of pyroclastic density current origin deduced by facies analysis and

- AMS flow directions. *Bull Volcanol* 70:1221–1236
- Gnojek I, Sedlák J, Rapprich V, Skácelová Z, Mlčoch B, Krentz O, Casas-García R (2018) Structure of the Carboniferous Altenberg–Teplice Caldera (Eastern part of the Krušné hory/Erzgebirge Mts.) revealed by combined airborne and ground gamma-ray spectrometry. *J Geosci* 63:3–20
- Gountié Dedzo M, Nédélec A, Nono A, Njanko T, Font E, Kamgang P, Njonfang E, Launeau P (2011) Magnetic fabrics of the Miocene ignimbrites from West-Cameroon: implications for pyroclastic flow source and sedimentation. *J Volcanol Geotherm Res* 203:113–132
- Grégoire V, de Saint Blanquat M, Nédélec A, Bouchez JL (1995) Shape anisotropy versus magnetic interactions of magnetite grains: experiments and application to AMS in granitic rocks. *Geophys Res Lett* 22:2765–2768
- Grégoire V, Darrozes J, Gaillot P, Nédélec A, Launeau P (1998) Magnetite grain shape fabric and distribution anisotropy vs rock magnetic fabric: a three-dimensional case study. *J Struct Geol* 20:937–944
- Gurioli L, Cioni R, Sbrana A, Zanella E (2002) Transport and deposition of pyroclastic density currents over an inhabited area: the deposits of the AD 79 eruption of Vesuvius at Herculaneum, Italy. *Sedimentology* 49:929–953
- Gurioli L, Pareschi MT, Zanella E, Lanza R, Deluca E, Bisson M (2005) Interaction of pyroclastic density currents with human settlements: evidence from ancient Pompeii. *Geology*, 33:441–444
- Haag MB, Sommer CA, Savian JF, Caselli AT, Moncinhatto TR, Hartmann GA, Ort MH, Poletti W, Trindade RIF (2021) AMS and rock magnetism in the Caviahue-Copahue Volcanic Complex (Southern Andes): emission center, flow dynamics, and implications to the emplacement of non-welded PDCs. *J Volcanol Geotherm Res* 416:107283. <https://doi.org/10.1016/j.jvolgeores.2021.107283>
- Hargraves RB, Johnson D, Chan CY (1991) Distribution anisotropy: the cause of AMS in igneous rocks? *Geophys Res Lett* 18:2193–2196
- Hargrove HR, Sheridan MF (1984) Welded tuffs deformed into megareomorphic folds during collapse of the McDermitt caldera, Nevada-Oregon. *J Geophys Res* 89:8629–8638
- Harrison RJ, Feinberg JM (2008) FORCinel: an improved algorithm for calculating first-order reversal curve distributions using locally weighted regression smoothing. *Geochem Geophys Geosy* 9:Q05016. doi:10.1029/2008GC001987
- Holub, FV (1980). Petrografický posudek vzorků ze strukturního vrtu Le –127. Czech Geol Surv, Prague
- Hong H, Chang L, Hayashida A, Roberts AP, Heslop D, Paterson GA, Kodoma K, Tauxe L (2019) Paleomagnetic recording efficiency of sedimentary magnetic mineral inclusions: implications for relative paleointensity determinations. *J Geophys Res Solid Earth* 124:6267–6279
- Hrouda F (1982) Magnetic anisotropy of rocks and its application in geology and geophysics. *Geophys Surv* 5:37–82
- Jelínek V, Kropáček V (1978) Statistical processing of anisotropy of magnetic susceptibility measured on groups of specimens. *Stud Geophys Geod* 22:50–62
- Jiránek J, Kříbek B, Mlčoch B, Procházka J, Schovánek P, Schováňková D, Schulmann K, Šebesta J, Šimůnek Z, Štemprok K (1987) Complex geological evaluation of the Teplice Rhyolite. Czech Geol Surv, Prague
- Knight M, Walker GPL, Ellwood BB, Diehl JF (1986) Stratigraphy, paleomagnetism, and magnetic fabric of the Toba tuffs: constraints on the sources and eruptive styles. *J Geophys Res* 91:10355–10382
- Kobberger H, Schmincke G (1999) Deposition of rheomorphic ignimbrite D (Mogán Formation), Gran Canaria, Canary Islands, Spain. *Bull Volcanol* 60:465–485
- LaBerge RD, Porreca M, Mattei M, Giordano G, Cas RAF (2009) Meandering flow of a pyroclastic density current documented by the anisotropy of magnetic susceptibility (AMS) in the quartz latite ignimbrite of the Pleistocene Monte Cimino volcanic centre (central Italy). *Tectonophysics* 466:64–78
- Lamarche G, Froggatt PC (1993) New eruptive vents for the Whakamaru ignimbrite (Taupo volcanic zone) identified from magnetic fabric study. *New Zeal J Geol Geophys* 36:213–222
- Le Pennec JL, Chen Y, Diot H, Froger JL, Gourgaud A (1998) Interpretation of anisotropy of magnetic susceptibility fabric of ignimbrites in terms of kinematic and sedimentological mechanisms: an Anatolian case-study. *Earth Planet Sci Lett* 157:105–127
- Lerner GA, Piispa EJ, Bowles JA, Ort MH (2022) Paleomagnetism and rock magnetism as tools for volcanology. *Bull Volcanol* 84:24 1–10. <https://doi.org/10.1007/s00445-022-01529-9>
- Levy RA (1968) Principles of solid state physics. Academic Press, New York and London.
- Lobin M (1986) Aufbau und Entwicklung des Permosiles im östlichen und mittleren Erzgebirge. Dissertation. Bergakademie Freiberg
- MacDonald WD, Palmer HC (1990) Flow directions in ash-flow tuffs: a comparison of geological and magnetic susceptibility measurements, Tshirege member (upper Bandelier Tuff), Valles caldera, New Mexico, USA. *Bull Volcanol* 53:45–59
- Martín-Hernández F, Hirt AM (2003) The anisotropy of magnetic susceptibility in biotite, muscovite and chlorite single crystals. *Tectonophysics* 367:13–28



- Mlčoch B, Skácelová Z (2010) Geometry of the Altenberg-Teplice Caldera revealed by the borehole and seismic data in its Czech part. *J Geosci* 55:217–229
- Moesta G (1928) Brüche und Porphyreffusionen im östlichen Erzgebirge. *Z Dtsch Geol Ges* 80:343–408
- Moncinhatto TR, Haag MB, Hartmann GA, Savian JF, Poletti W, Sommer CA, Caselli AT, Trindade RIF (2019) Mineralogical control on the magnetic anisotropy of lavas and ignimbrites: a case study in the Caviahue-Copahue field (Argentina). *Geophys J Int* 220:821–838
- Opluštil S, Schmitz M, Cleal CJ, Martínek K (2016) A review of the Middle-Late Pennsylvanian west European regional substages and floral biozones, and their correlation to the Geological Time Scale based on new U-Pb ages. *Earth-Science Rev* 154:301–335
- Ort MH, Rosi M, Anderson CD (1999) Correlation of deposits and vent locations of the proximal Campanian Ignimbrite deposits, Campi Flegrei, Italy, based on natural remanent magnetization and anisotropy of magnetic susceptibility characteristics. *J Volcanol Geotherm Res* 91:167–178
- Ort MH, Orsi G, Pappalardo L, Fisher RV (2003) Anisotropy of magnetic susceptibility studies of depositional processes in the Campanian Ignimbrite, Italy. *Bull Volcanol* 65:55–72
- Ort MH, De Silva SL, Jiménez C. N, Jicha BR, Singer BS (2013) Correlation of ignimbrites using characteristic remanent magnetization and anisotropy of magnetic susceptibility, Central Andes, Bolivia. *Geochem, Geophys Geosy* 14:141–157
- Ort MH, Newkirk TT, Vilas JF, Vazquez JA (2015) Towards the definition of AMS facies in the deposits of pyroclastic density currents. *Geol Soc Spec Publ* 396:205–226
- Petronis MS, Geissman JW (2009) Anisotropy of magnetic susceptibility data bearing on the transport direction of mid-tertiary regional ignimbrites, Candelaria Hills area, West-Central Nevada. *Bull Volcanol* 71:121–151
- Pfeiffer T (2001) Vent development during the Minoan eruption (1640 BC) of Santorini, Greece, as suggested by ballistic blocks. *J Volcanol Geoth Res* 106:229–242
- Pioli L, Lanza R, Ort MH, Rosi M (2008) Magnetic fabric, welding texture and strain fabric in the Nuraxi Tuff, Sardinia, Italy. *Bull Volcanol* 70:1123–1137
- Platzman ES, Sparks RSJ, Cooper FJ (2020) Fabrics, facies, and flow through a large-volume ignimbrite: Pampa De Oxaya, Chile. *Bull Volcanol* 82:1–19
- Potter DK, Stephenson A (1988) Singledomain particles in rocks and magnetic fabric analysis. *Geophys Res Lett* 15:1097–1100
- Pueyo Anchuela O, Gil Imaz A, Gil-Peña I, Maestro A, Galindo-Zaldivar J, López-Martínez, Rey J, Soto R, Oliva-Urcia B (2014) Application of AMS for reconstruction of the geological evolution of recent volcanic systems: case of Deception Island (South Shetland Islands, Antarctica). *Tectonophysics* 626:69–85
- Roberts AP, Cui Y, Verosub KL (1995) Wasp-waisted hysteresis loops: mineral magnetic characteristics and discrimination of components in mixed magnetic systems. *J Geophys Res Solid Earth* 100:17909–17924
- Roberts AP, Pike CR, Verosub KL (2000) First-order reversal curve diagrams: a new tool for characterizing the magnetic properties of natural samples. *J Geophys Res Solid Earth* 105:28461–28475
- Roche O, Buesch DC, Valentine GA (2016) Slow-moving and far-travelled dense pyroclastic flows during the Peach Spring super-eruption. *Nat Commun* 7:1–8
- Roche O, Druitt TH (2001) Onset of caldera collapse during ignimbrite eruptions. *Earth Planet Sci Lett* 191:191–202
- Rochette P, Jackson M, Aubourg C (1992) Rock magnetism and the interpretation of anisotropy of magnetic susceptibility. *Rev Geophys* 30:209–226
- Rochette P, Fillion G, Mattei JL, Dekkers MJ (1990) Magnetic transition at 30-34-Kelvin in pyrrhotite: insight into a widespread occurrence of the mineral in rocks. *Earth Planet Sc Lett* 98:319–328
- Rochette P, Aubourg C, Perrin M (1999) Is this magnetic fabric normal? A review and case studies in volcanic formations. *Tectonophysics* 307:219–234
- Ross CS, Smith RL (1961) Ash-flow tuffs: their origin, geologic relations, and identification. USGS Prof Pap 366. <https://doi.org/10.3133/pp366>
- Schovánek P (2004) Vysvětlivky k základní geologické mapě České republiky 1:25 000, sheets 02-321 and 02-143. *Czech Geol Surv, Prague*
- Sohn YK, Son M, Jeong JO, Jeon YM (2009) Eruption and emplacement of a laterally extensive, crystal-rich, and pumice-free ignimbrite (the Cretaceous Kusandong Tuff, Korea). *Sediment Geol* 220:190–203
- Sparks RSJ (1976) Grain size variations in ignimbrites and implications for the transport of pyroclastic flows. *Sedimentology* 23:147–188
- Sparks RSJ, Wilson L (1976) A model for the formation of ignimbrite by gravitational column collapse. *J Geol Soc London* 132:441–451
- Sparks RSJ, Self S, Walker GPL (1973) Products of ignimbrite eruptions. *Geology* 1:115–118
- Štemprok M (2016) Drill hole CS-1 penetrating the Cínovec/Zinnwald granite cupola (Czech Republic): an A-type granite with important hydrothermal mineralization. *J Geosci* 61:395–423

- Štemprok M, Holub FV, Novák JK (2003) Multiple magmatic pulses of the Eastern Volcano-Plutonic Complex, Krušné hory/Erzgebirge batholith, and their phosphorus contents. *Bull Geosci* 78:277–296
- Štemprok M, Dolejš D, Holub FV (2014) Late Variscan calc-alkaline lamprophyres in the Krupka ore district, Eastern Krušné hory/Erzgebirge: their relationship to Sn-W mineralization. *J Geosci-Czech* 59:41–68
- Stephenson A (1994) Distribution anisotropy: two simple models for magnetic lineation and foliation. *Phys Earth Planet Inter* 82:49–53
- Tarling DH, Hrouda F (1993) *Magnetic anisotropy of rocks*. Chapman & Hall, London
- Tichomirowa M, Kášner A, Repstock A, Weber S, Gerdes A, Whitehouse M (2022) New CA-ID-TIMS U-Pb zircon ages for the Altenberg Teplice Volcanic Centre (ATVC) document discrete and coeval pulses of Variscan magmatic activity in the Eastern Erzgebirge (Eastern Variscan Belt). *Int J Earth Sci*, in press
- Tomek F, Žák J, Svojtka M, Finger F, Waitzinger M (2019) Emplacement dynamics of syn-collapse ring dikes: an example from the Altenberg-Teplice caldera, Bohemian Massif. *GSA Bull* 131:997–1016
- Tomek F, Opluštil S, Svojtka M, Špillar V, Rappich V, Míková J (2022) Altenberg–Teplice Caldera sourced Westphalian fall tuffs in the central and western Bohemian Carboniferous basins (eastern Variscan belt). *Int Geol Rev* 64: 441–468
- Van Den Bogaard P, Schmincke HU (1984) The eruptive center of the late quaternary Laacher see tephra. *Geol Rundsch* 73:933–980
- Verwey EJW and Haayman PW (1941) Electronic conductivity and transition point of magnetite (“Fe<sub>3</sub>O<sub>4</sub>”), *Physica*, 8:979–987
- Walker GPL (1983) Ignimbrite types and ignimbrite problems. *J Volcanol Geotherm Res* 17:65–88
- Wang X, Roberts J, Schmidt P (2001) Flow directions of carboniferous ignimbrites, Southern New England Orogen, Australia, using anisotropy of magnetic susceptibility. *J Volcanol Geotherm Res* 110:1–25
- Willcock MAW, Mattei M, Hasalová P, Giordano G, Cas RAF, Morelli C (2015) Flow behaviour in the intra-caldera setting: an AMS study of the large (> 1290 km<sup>3</sup>) Permian Ora ignimbrite. *Geol Soc London Spec Publ* 396:177–204
- Wilson CJN, Hildreth W (2000) The Bishop Tuff: new insights from eruptive stratigraphy. *J Geol* 105:407–439
- Winter C, Breikreuz C, Lapp M (2008) Textural analysis of a Late Palaeozoic coherent-pyroclastic rhyolitic dyke system near Burkersdorf (Erzgebirge, Saxony, Germany). *Geol Soc Spec Publ* 302:199–221
- Žáček V, Škoda R (2009) Petrology of crystalline rocks in the geothermal borehole GTPV-LT1 in Litoměřice. *Geosci Res Rep* 205–212
- Žák J, Tomek F, Svojtka M, Vacek F, Kachlík V, Ackerman A, Ježek J, Petronis MS (2021) Distributed crustal shortening followed by transpressional shearing in the Superior Province, northeastern Canada: a Late Archean analogy to modern accretionary plate margins? *Precambrian Res* 362: 106322. <https://doi.org/10.1016/j.precamres.2021.106322>